Received: 14 October 2020 | Revised: 12 February 2021 | Accepted: 14 February 2021

DOI: 10.1111/gbi.12438

ORIGINAL ARTICLE

gebiology WILEY

Anoxygenic photosynthesis linked to Neoarchean iron formations in Carajás (Brazil)

Eric Siciliano Rego[1,2,3] | Vincent Busigny[2] | Stefan V. Lalonde[4] | Pascal Philippot[2,3,5] | Amaury Bouyon[3] | Camille Rossignol[2,5] | Marly Babinski[1] | Adriana de Cássia Zapparoli[6]

[1]Instituto de Geociências, Universidade de São Paulo, Cidade Universitária, São Paulo, Brazil

[2]Institut de Physique du Globe de Paris, Université de Paris, CNRS, Paris cedex 05, France

[3]Géosciences Montpellier, Université de Montpellier, CNRS, Université des Antilles, Montpellier, France

[4]Institut Universitaire Européen de la Mer, Université de Bretagne Occidentale, CNRS, Plouzané, France

[5]Departamento de Geofísica, Instituto de Astronomia, Geofísica e Ciências Atmosféricas, Universidade de São Paulo, Cidade Universitária, São Paulo, Brazil

[6]Vale S.A, CTF, Nova Lima, Brazil

Correspondence
Eric S. Rego, Instituto de Geociências, Universidade de São Paulo, Rua do Lago 562, Cidade Universitária, São Paulo, 05508-080, Brazil; Géosciences Montpellier, Université de Montpellier, CNRS, Université des Antilles, 34095, Montpellier, France.
Email: ersiciliano@usp.br

Funding information
Fundação de Amparo à Pesquisa do Estado de São Paulo, Grant/Award Number: 2019/16271-0, 2018/05892-0, 2015/16235-2 and 2018/02645-2

Abstract

Microbial activity is often invoked as a direct or indirect contributor to the precipitation of ancient chemical sedimentary rocks such as Precambrian iron formations (IFs). Determining a specific metabolic pathway from the geological record remains a challenge, however, due to a lack of constraints on the initial conditions and microbially induced redox reactions involved in the formation of iron oxides. Thus, there is ongoing debate concerning the role of photoferrotrophy, that is the process by which inorganic carbon is fixed into organic matter using light as an energy source and Fe(II) as an electron donor, in the deposition of IFs. Here, we examine ~2.74-Ga-old Neoarchean IFs and associated carbonates from the Carajás Mineral Province, Brazil, to reconstruct redox conditions and to infer the oxidizing mechanism that allowed one of the world's largest iron deposits to form. The absence of cerium (Ce) anomalies reveals that conditions were pervasively anoxic during IF deposition, while unprecedented europium (Eu) anomalies imply that Fe was supplied by intense hydrothermal activity. A positive and homogeneous Fe isotopic signal in space and time in these IFs indicates a low degree of partial oxidation of Fe(II), which, combined with the presence of ^{13}C-depleted organic matter, points to a photoautotrophic metabolic driver. Collectively, our results argue in favor of reducing conditions during IF deposition and suggest anoxygenic photosynthesis as the most plausible mechanism responsible for Fe oxidation in the Carajás Basin.

KEYWORDS

anoxygenic photosynthesis, Carajás, Fe isotopes, iron formations, Neoarchean

1 | INTRODUCTION

The geological record preserves extensive deposits of iron-rich chemical sediments, referred to as iron formations (IFs). These rocks are characterized by a high content (>15%–20%) of iron-bearing minerals, typically layered or massive, interbedded with silica and/or carbonate-rich layers that were deposited throughout the Precambrian (James, 1983; Klein, 2005). Over the past few decades, studies have employed the chemical and isotopic composition of IFs to constrain past environmental conditions (e.g., Planavsky et al., 2014; Satkoski et al., 2015) and to understand how the microbial iron cycle evolved alongside redox conditions through time (Heard & Dauphas, 2020; Johnson et al., 2008; Rouxel, 2005). Even though there is still ongoing debate as to how IFs are formed, most models rely on either oxygenic and/or anoxygenic photosynthesis, or abiotic photochemical oxidation by UV radiation, as the main process that allowed ferrous iron [Fe(II)]

to be oxidized and removed from ferruginous waters and subsequently deposited as mixed valence iron (oxyhydr)oxides and carbonates (Thompson et al., 2019) [see Tosca et al. (2016) for alternative model]. A combination of experiments and thermodynamic models has shown that UV photo-oxidation of Fe(II) could have made important contributions to IF precipitation, but was not likely a major oxidizing mechanism for the deposition of large IFs (Konhauser et al., 2007; Pecoits et al., 2015). If correct, these results would point to microbial activity, either through oxygenic or anoxygenic photosynthesis, as the main oxidizing mechanism (Kappler & Newman, 2004; Konhauser et al., 2002).

Recent studies have argued that anoxygenic photosynthesis could be the evolutionary predecessor of oxygenic photosynthesis (e.g., Blankenship et al., 2007; Fischer et al., 2016; Martin et al., 2018; Hamilton, 2019) and that photoferrotrophic microorganisms likely played a significant role in nutrient cycling as primary producers prior to the rise of atmospheric oxygen ~2.4 billion years (Ga) ago, the so-called the Great Oxidation Event (GOE) (Canfield et al., 2006; Holland, 2006; Jones et al., 2015; Thompson et al., 2017). Accordingly, the hypothesis that IF deposition may have been driven by oxidation of Fe(II) via anoxygenic photosynthesis has received significant attention, particularly to explain IF deposition during periods of low oxygen concentrations such as the Archean Eon (Canfield et al., 2000; Farquhar et al., 2000; Konhauser et al., 2002; Widdel et al., 1993). Photoferrotrophs utilize Fe(II) as an electron donor and light energy to fix inorganic carbon into biomass and produce Fe(III) as a metabolic by-product as illustrated by the following reaction:

$$CO_2 + 4Fe^{2+} + 11H_2O \rightarrow {}^{hv}CH_2O + 4Fe(OH)_3 + 8H^+ \quad (1)$$

Despite observations of these organisms performing iron oxidation in modern environments (e.g., Archean analogs; Crowe et al., 2008; Llirós et al., 2015) and a vast bibliography arguing in favor of photoferrotrophy as a potential mechanism that allowed IFs to form under oxygen-free conditions (e.g., Croal et al., 2009; Czaja et al., 2013, 2018; Gauger et al., 2015, 2016; Johnston et al., 2009; Thompson et al., 2019), there is still little evidence reported from the geological record supporting Fe oxidation by photoferrotrophs. Here, we combined Fe and C stable isotopes with trace element analyses of two pristine drill cores intercepting well-preserved Neoarchean IFs from the Carajás Mineral Province, Brazil, and show that photoferrotrophs played a key role in IF deposition, particularly under anoxic and ferruginous conditions. Considering that the two drill cores investigated are 50 km away from each other, we suggest that anoxygenic photosynthesis was the main oxidizing pathway that allowed these rocks to form at the scale of the Carajás Basin, which is one of the major iron-rich deposits in Brazil.

Summary Statement

Iron formations (IFs) deposited throughout the globe require an oxidizing mechanism to transform hydrothermally sourced Fe(II) into Fe(III). Debate is ongoing concerning the role of anoxygenic photosynthesis in the deposition of IFs prior to the rise of atmospheric oxygen. We provide geochemical evidence for pervasively anoxic conditions with continuous hydrothermal influence during the deposition of the Carajás Mineral Province, the largest Neoarchean IFs worldwide. The carbon isotope composition of organic matter indicates the presence of autotrophic organisms. Together with Fe isotope data indicating only small degrees of oxidation of the Fe(II) pool, our results suggest that Fe-oxidizing bacteria were the main agent for iron oxidation via anoxygenic photosynthesis. This supports a strong role for photoferrotrophs during IF deposition and reinforces their significance in the metabolic landscape prior to the Great Oxidation Event.

2 | GEOLOGICAL SETTING

The Carajás Mineral Province (CMP) is located in the southeastern part of the Amazonian Craton, Brazil (Figure 1a), and contains remarkable metallogenic diversity including world-class deposits of iron oxide–copper–gold (IOCG), large IFs, and Mn ore (Klein & Ladeira, 2002; Moreto et al., 2015). The Carajás Basin, within the CMP (Figure 1b), has a Mesoarchean (c. 3.0–2.86 Ga) basement composed of mafic granulites, migmatites, and metavolcanic rocks (Machado et al., 1991). The crystalline basement is overlain unconformably by Neoarchean and Paleoproterozoic volcano-sedimentary sequences from the Grão Pará Group that have undergone subgreenschist to low-greenschist facies metamorphism (Krymsky et al., 2007; Machado et al., 1991; Rosière et al., 2006). The volcano-sedimentary sequences are composed initially by basalts and basaltic andesites of the Parauapebas Formation, while IFs from the Carajás Formation conformably overlie or are occasionally interlayered with the basalts, a typical characteristic of Algoma-type IFs (Dalstra & Guedes, 2004; Klein & Ladeira, 2002; Martins et al., 2017). The main lithology comprising the Carajás Formation are oxide facies banded iron formations alternating between iron-rich and chert layers, but minor black shales and conglomeratic layers have also been reported (Cabral et al., 2013, 2017). These were interpreted to have been deposited in a range of environments from shallow water, low-energy environments, to deep and quiet water settings (Lindenmayer et al., 2001; Macambira & Schrank, 2002; Ribeiro da Luz & Crowley, 2012; Tolbert et al., 1971).

A Late Archean to Early Paleoproterozoic sedimentary cover overlies the IFs; however, its age is still debated (Rossignol et al., 2020). The depositional age of the Carajás IFs is well constrained by U-Pb zircon ages of c. 2.755–2.740 Ga in the basalts underlying and intercalating the IFs (Gibbs et al., 1986; Krymsky et al., 2007; Machado et al., 1991) and U-Pb zircon ages from a possible tuff (2,743 ± 11 Ma) and a dolerite dyke (2,740 ± 8 Ma) cross-cutting the Carajás Formation (Trendall et al., 1998). Other age

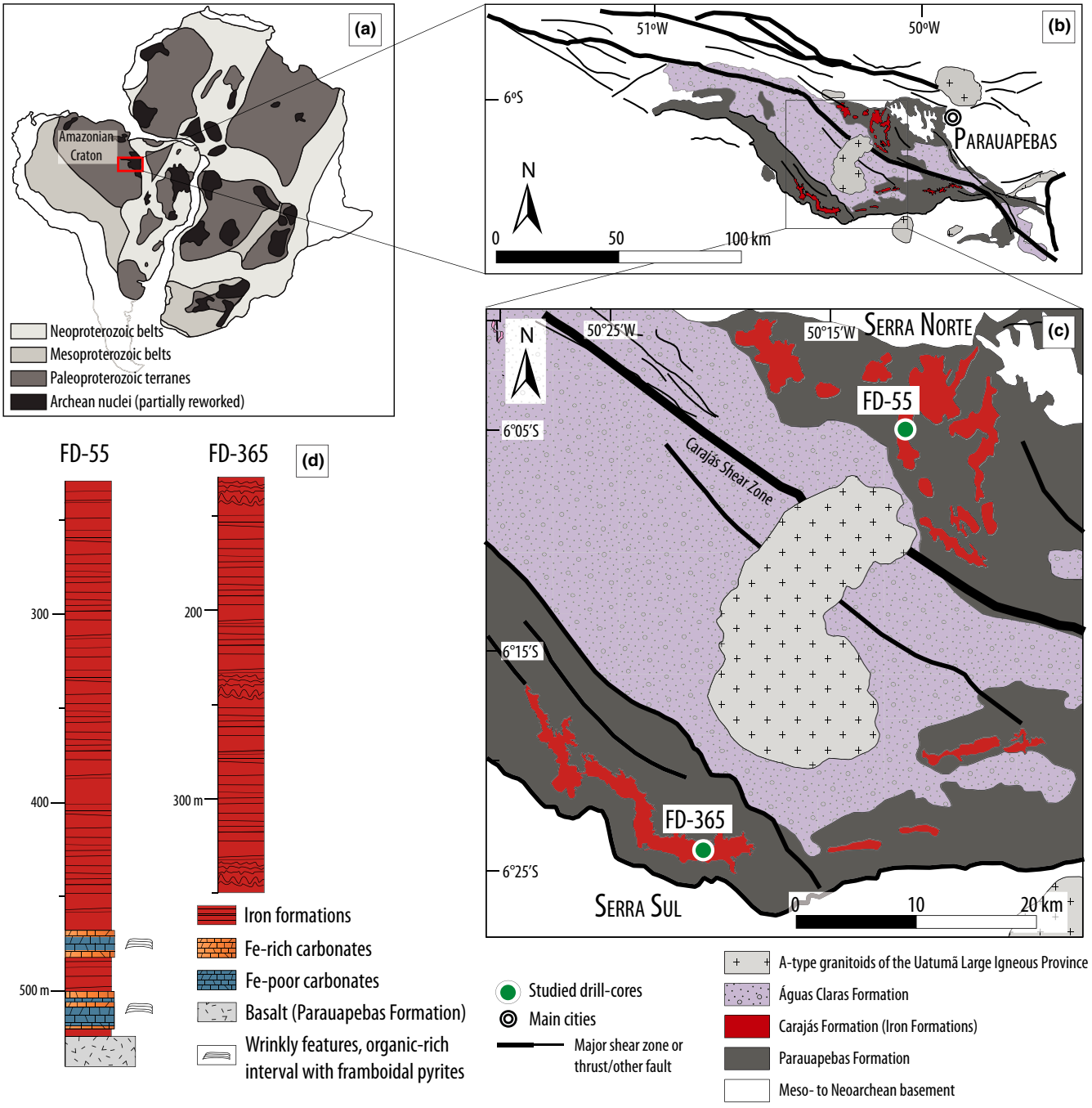

FIGURE 1 Geological map of the Carajás Mineral Province within the Amazonian Craton (a) and its relation to the São Francisco and West-African Cratons, highlighting the main lithological components of the Carajás Basin (b, c) and the positions of the studied drill cores FD-55 and FD-365 in Serra Norte and Serra Sul, respectively

constraints include a Sm-Nd age of c. 2,593 ± 260 Ma in jaspilites from Serra Norte (Lindenmayer et al., 2001) and two Re-Os ages of 2,661 ± 110 Ma and 2,710 ± 38 Ma in black shales intercalated with IFs in Serra Sul (Cabral et al., 2013). The iron deposits have an average thickness of 200–250 m in the Serra Norte and 300 m in the Serra Sul regions (Beisiegel et al., 1973), and pristine drill cores intercepting the IFs were selected from each locality (FD-55 and FD-365, respectively), spanning a distance of 50 km, to examine spatial variations in the basin (Figure 1c).

3 | MATERIALS AND METHODS

3.1 | Mineralogy

The mineralogy was determined using thin sections examined by reflected and transmitted light microscopy at the Université de Montpellier, complemented by scanning electron microscopy (SEM) and energy-dispersive X-ray spectroscopy (EDS) using a Zeiss EVO MA10 SEM for semi-quantitative *SEM*-EDS analysis at

the Institut de Physique du Globe de Paris (IPGP). Standard operating conditions for SEM imaging and EDS analyses were 15 kV accelerating voltage, working distance of 12 mm, and electron beam current of 2–3 nA. Samples were coated with C prior to analysis.

3.2 | Major elements

Approximately 250 mg of rock powder was dissolved in closed teflon vessel (Savillex) at about 90°C for one day using 3 ml of concentrated HF (40%), 3 ml of concentrated HCl (32%), and 1 ml of concentrated HNO_3 (65%). Afterward, 93 ml of H_3BO_3 aqueous solution (20 g/L H_3BO_3) was added to neutralize the excess HF. All reagents used were graded analytically. Elements were measured by inductively coupled plasma atomic emission spectrometry (ICP-AES) using a Horiba Jobin Yvon® Ultima 2 spectrometer at the PSO/IUEM (Pôle Spectrométrie Océan, Institut Universitaire Européen de la Mer, Brest, France), following the analytical procedure of Cotten et al. (1995). The boron included in the solution was used as an internal standard. The precision and accuracy were evaluated using international standards IF-G, ACE, JB2, and WSE. The relative standard deviation was ≤ 1% for SiO_2 and ≤2% for the other major elements.

3.3 | Trace elements

Between 80 and 100 mg of powdered samples was dissolved using a mixture of concentrated HF-HNO_3, evaporated to dryness, and re-dissolved in Aqua Regia solution, all in PFA beakers heated to 80°C in a class 1,000 clean laboratory. The residues were then re-dissolved in 5 ml 6 M HCl overnight at 80°C and archived. Splits of 100 µl from the archive solutions were taken up in 5 ml ~ 0.28 M HNO_3 for ICP-MS measurements. Two geostandards (BHVO-2 and CAL-S) and a procedural blank were also prepared with the samples. Elemental concentrations were measured with a HR-ICP-MS Element XR (Thermo Fisher Scientific) at the PSO/IUEM (Pôle Spectrométrie Océan, Institut Universitaire Européen de la Mer, Brest, France) using indium as an internal standard for correcting drift of the signal during analysis. Concentrations were calibrated using serially diluted mixtures of commercial NIST-traceable ICP-MS calibration standards (SPEX CertiPrep) prepared gravimetrically for the analyses. Results on the geostandards were within the range published in the literature.

3.4 | Fe isotopes

The method applied here for Fe isotope measurement was described in a previous contribution (Busigny et al., 2014). Approximately 10–30 mg of powdered samples was dissolved with mixtures of HF, HCl, HNO_3, and eventually additional $HClO_4$ depending on the sample composition, to ensure complete digestion and that all iron was in its ferric state. Iron was separated from other elements in the sample matrix by anion exchange chromatography (Strelow, 1980) to avoid mass bias in the mass spectrometer and to eliminate elements generating potential isobaric interferences on Fe masses. This procedure was repeated twice for each sample to assure that all matrix elements were eliminated (Dauphas, Janney, et al., 2004). Bio-Rad Poly-Prep columns were filled with 1 ml anion exchange resin (AG1-X8 200-400 mesh chloride form). The resin was cleaned three times with 10 ml H_2O and 5 ml 1 M HNO_3. It was then preconditioned in HCl medium by running 10 ml H_2O, 10 ml 0.4 M HCl, 5 ml H_2O, and 2 ml 6 M HCl. Depending on the sample (IF or carbonates), half or one third (300 µl or 200 µl, respectively) of the sample solution was loaded on the column in 6 M HCl. Matrix elements were eluted with 8 ml 6 M HCl, whereas Fe(III) was strongly adsorbed on the resin and quantitatively retained. Fe was subsequently eluted in 10 ml 0.4 M HCl. The Fe blank level of the present procedure has been evaluated by systematic analyses of one blank in each sample series, prepared as described above but without any sample powder. The blank was always below 30 ng Fe (average ~20 ng), thus representing less than 0.3% of the bulk Fe.

Iron isotope compositions were measured using a Neptune Plus™ Thermo Fisher MC-ICP-MS (multiple-collector inductively coupled plasma mass spectrometer) at the Institut de Physique du Globe de Paris (IPGP). The samples were analyzed in 0.3 M HNO_3 at a concentration of ~2 ppm Fe. Iron isotopes were fully resolved from argide interferences using the high-resolution mode of the Neptune (Schoenberg & Von Blanckenburg, 2005; Weyer & Schwieters, 2003). Instrumental mass discrimination was corrected for using the conventional sample-standard bracketing (SSB) approach (Rouxel et al., 2003). The $^{56}Fe/^{54}Fe$ and $^{57}Fe/^{54}Fe$ ratios were expressed in the usual δ notation in per mil (‰) as,

$$\delta^{56}\mathrm{Fe} = \left[\left(^{56}\mathrm{Fe}/^{54}\mathrm{Fe}\right)_{\mathrm{sample}}/\left(^{56}\mathrm{Fe}/^{54}\mathrm{Fe}\right)_{\mathrm{standard}} - 1\right] \times 1{,}000.$$

$$\delta^{57}\mathrm{Fe} = \left[\left(^{57}\mathrm{Fe}/^{54}\mathrm{Fe}\right)_{\mathrm{sample}}/\left(^{57}\mathrm{Fe}/^{57}\mathrm{Fe}\right)_{\mathrm{standard}} - 1\right] \times 1{,}000.$$

where the standard is IRMM-014, a pure synthetic Fe metal from the Institute for Reference Materials and Measurements (Taylor et al., 1992). Based on replicate analyses of IRMM-014 and international rock geostandard IF-G (a banded iron formation from Isua, Greenland), the external precision was always better than 0.05‰ for δ^{56}Fe and 0.08‰ for δ^{57}Fe (2σ). IF-G isotope measurements provided δ^{56}Fe and δ^{57}Fe values of 0.616 ± 0.025‰ and 0.886 ± 0.079‰, respectively (2σ; 8 measurements of four digested powders), in good agreement with recommended values (Craddock & Dauphas, 2011; Dauphas et al., 2009).

3.5 | Organic carbon isotopes

Total organic carbon (TOC) content and isotope composition were determined on decarbonated samples. Carbonates from powdered samples were removed using 6N HCl and a chromium chloride

reducing solution for 2 hr at 80°C, following the method from Muller et al. (2017). The residue was rinsed with distilled water and centrifuged several times until neutral pH was reached, and then dried at 50°C for 2 days. After drying, the decarbonated powders were weighed and mass balance was done for subsequent calculation of the total organic C content. The powders were ground again in an agate mortar to avoid any heterogeneity related to the decarbonation procedure. Aliquots of dried decarbonated samples (50–100 mg) were weighed and sealed in tin capsules. All capsules were analyzed on a Flash EA1112 elemental analyzer coupled to a Thermo Finnigan Deltaplus XP mass spectrometer via a ConFlo IV interface under a helium continuous flow. All samples were measured once to estimate the organic content, then weighed (10–140 mg) to get an approximate intensity of 6V on m/z 44. Three internal standards (1 graphite "LC", 1 anthracite "GR," and 1 organic soil sample "CAP") were calibrated against international standards and used to calculate the $\delta^{13}C$ values of all samples. Standards were measured every six samples to monitor and correct for a potential drift. Blanks were evaluated with empty capsules, yielding negligible contribution to the total signal. Replicate analyses on standards gave an external precision better than ±0.1‰ (1σ). Five different amounts (from 1 to 6μmol, corresponding to approximately 2 to 12V on m/z = 44) of an internal standard were used to estimate total organic C content of the samples (Cheng et al., 2019). The data were reported using the conventional δ unit (in per mil) with respect to the V-PDB standard, such as,

$$\delta^{13}C_{org} = \left[\left(^{13}C/^{12}C\right)_{sample}/\left(^{13}C/^{12}C\right)_{standard} - 1\right] \times 1{,}000.$$

At least three replicate analyses of each sample were performed for $\delta^{13}C_{org}$ and organic content measurements, but only the average values are provided herein. The reproducibility on samples' TOC content and $\delta^{13}C_{org}$ values was always better than ±0.08 wt.% (1σ) and ±0.4‰ (1σ), respectively.

4 | RESULTS

The two cores studied (FD55 and FD365) consist of finely laminated jaspilites formed by mm-scale laminae of chert (e.g., microcrystalline quartz) intercalated with euhedral magnetite and red jasper. Spherulitic hematite and minor amounts of ankerite occur disseminated in the chert matrix (Figure 2a–c). A major difference between the two cores is the occurrence of two main carbonate intervals present only in core FD-55 that are so far the oldest carbonates reported in South America. Two main types of carbonate are present: i) Fe-rich carbonates composed dominantly of ankerite and microcrystalline quartz intercalated with magnetite layers (Figure 2d–g) and ii) Fe-poor carbonates composed of calcite, ankerite, and rare finely laminated magnetite layers locally displaying wrinkly-laminated features (Figure 2h–l). Framboidal pyrites are common in Fe-poor carbonate intervals, particularly in the wrinkly-laminated samples, which are usually associated with the presence of organic matter (Figure 2i–j). Minor amounts of Fe-silicates (e.g., stilpnomelane and minnesotaite) are also present in the Fe-poor carbonate layers.

Iron formations from both cores have very low abundances of poorly mobile elements, including Al, Ti, Zr, Th, and Hf. Al contents in IFs range from 0.02 to 0.2 wt.% (mean = 0.06 wt.%, $n = 15$), while Ti, Zr, and Th concentrations are below 70, 21, and 0.25 ppm, respectively. Iron-rich and iron-poor carbonates show an enrichment in Al compared with IFs, with concentrations slightly below 1 wt.% for the most enriched samples (mean Al content in carbonate is 0.17 wt.%, $n = 24$; Figure 3). Only IFs and carbonates with Al content below 0.2 wt.% will be considered in the following discussion to avoid potential detrital contribution and focus on the purely chemical and authigenic signatures of the sediment. In general, rare earth element and yttrium (REY) data normalized to post-Archean Australian shale (PAAS; McLennan, 1989) show positive La, Eu, and Y anomalies in IFs and carbonates. Cerium anomalies (Ce/Ce*) were calculated according to Bau and Dulski (1996) using the projection between La and Pr, but evaluated against Pr/Pr* to distinguish false Ce anomalies arising from the presence of positive La anomalies, which occur in our sample set (Figure 4). No significant true Ce anomalies, either positive or negative, were observed among the studied samples (Figure 5). Positive Eu anomalies (Eu/Eu*) are highly variable, with several extreme values up to 18. Relative abundances of Y are also very high, with an average Y/Ho ratio that is strongly super-chondritic at 83.3 ($n = 56$). The light REY (LREY) is not depleted relative to the heavy REY (HREY) as demonstrated by the ratio Pr/Yb_{sn} with an average value of 1.06 ($n = 56$).

The iron isotope compositions of the IFs are remarkably homogeneous throughout the two drill core depth intervals (~ 200 and 150 m depths) and show an enrichment in the heavier isotope with $\delta^{56}Fe$ values ranging from +1.03 to +1.95‰ with an average of +1.39 ± 0.22 (1σ, $n = 27$). Iron-rich and Fe-poor carbonates show distinct $\delta^{56}Fe$ values of +0.2 to +0.8‰ and −0.4 to +0.07‰, respectively, and one anomalous Fe-rich carbonate sample with −0.8‰. The isotopic composition of organic carbon in IFs and carbonates shows significant variability, with $\delta^{13}C_{org}$ values from −23.50 to −28.17‰ and −21.17 to −31.80‰, respectively, and an average $\delta^{13}C_{org}$ value of −25.5 ± 2.7‰ (1σ, $n = 15$).

5 | DISCUSSION

5.1 | Anoxic conditions during IF deposition in the Carajás basin

Shale-normalized rare earth element and yttrium (REY) data are extensively used as a geochemical tool to characterize conditions in which IFs were formed (Planavsky et al., 2010). In modern seawater and marine sediments, the REY system is controlled by terrestrial versus hydrothermal inputs and particle-solution interactions that are susceptible to change with salinity, water depth, and redox state (Robbins, Konhauser, et al., 2019). Similarities between REY patterns from modern environments and the geological record imply


1 cm
(a)

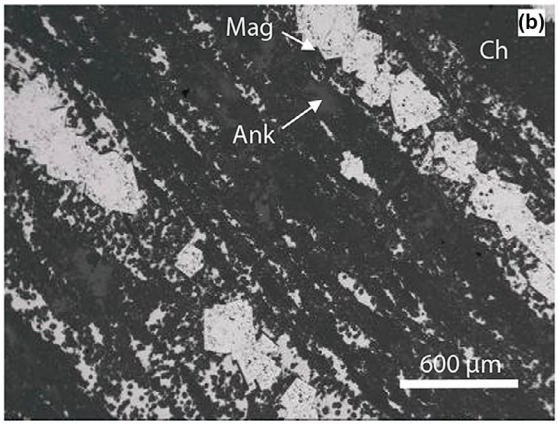
Mag
Ank
Ch
(b)
600 µm

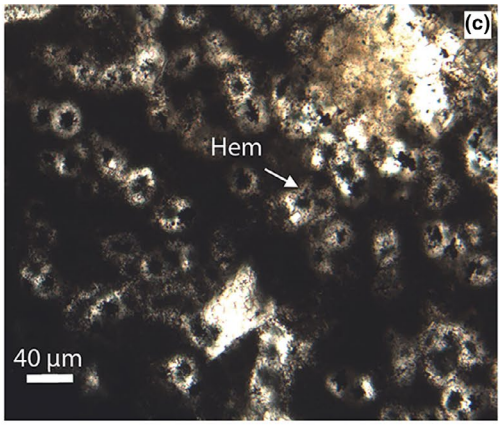
Hem
(c)
40 µm


1 cm
(d)

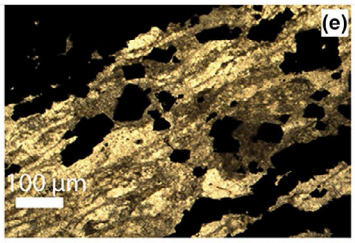
(e)
100 µm

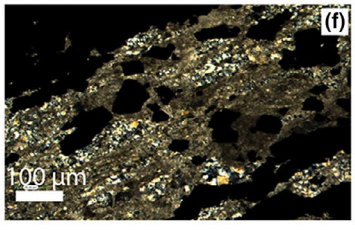
(f)
100 µm

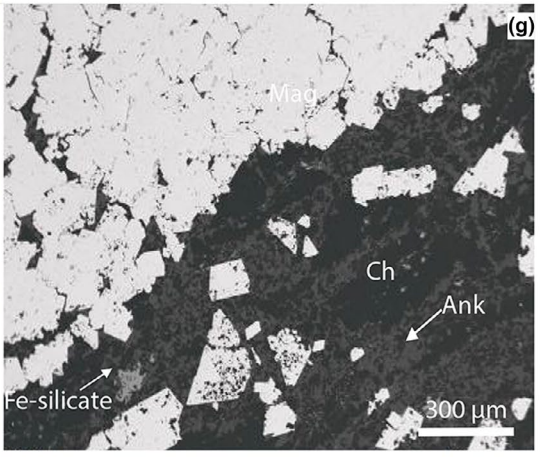
Mag
Ch
Ank
Fe-silicate
(g)
300 µm


1 cm
(h)

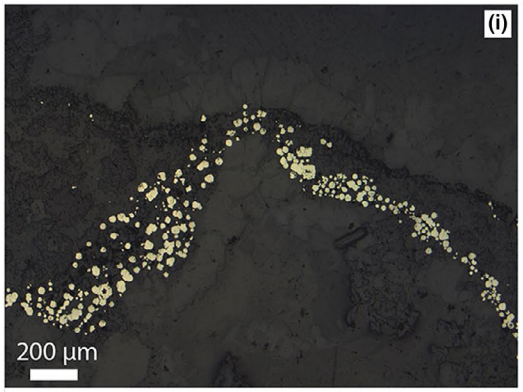
(i)
200 µm

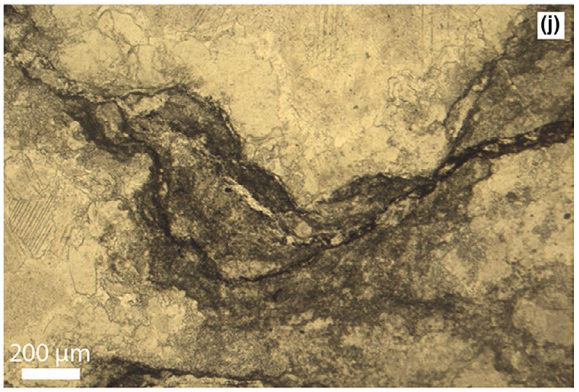
(j)
200 µm


1 cm
(k)

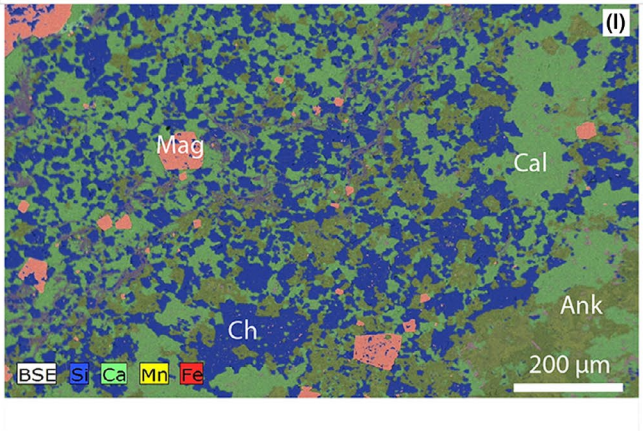
Mag
Cal
Ank
Ch
BSE Si Ca Mn Fe
(l)
200 µm

FIGURE 2 Different facies among both studied cores (FD-55 and FD-365) showing IFs being represented by finely laminated jaspilites formed by mm-scale laminae of chert (e.g., microcrystalline quartz) intercalated with euhedral magnetite and red jasper with spherulitic hematite and minor amounts of ankerite disseminated in the chert matrix (a–c). Fe-rich carbonates composed dominantly of ankerite and microcrystalline quartz intercalated with magnetite layers (d–g) and Fe-poor carbonates composed of calcite, ankerite, and rare finely laminated magnetite layers locally displaying wrinkly-laminated features (h–l). Framboidal pyrites are commonly present in the Fe-poor carbonate interval, particularly in the wrinkly-laminated features, which are usually associated with organic matter (i, j)

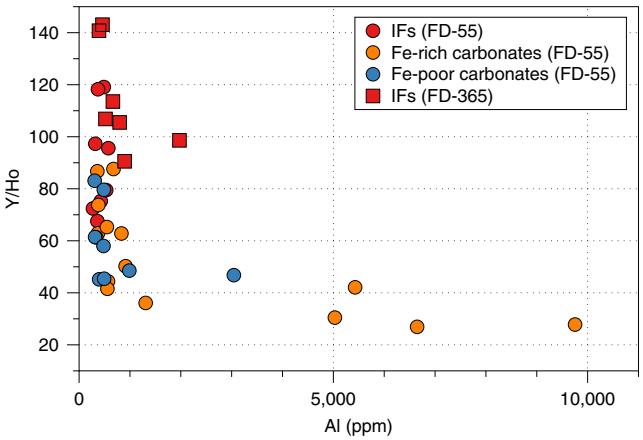

FIGURE 3 Detrital-free IFs shown by low concentrations of Al and super-chondritic Y/Ho values

the preservation of a primary seawater signature from which these rocks were formed (Oonk et al., 2018). Detrital contamination, however, has been proven to mute or mask primary signals, but is easily identified by increasing concentration of poorly mobile elements such as Al, Ti, Sc, Zr, U, Th, or Hf. Additionally, the influence of post-depositional processes (e.g., diagenesis and metamorphism) does not alter significantly the primary REY composition of IFs (Bau & Möller, 1993). The IFs from Carajás studied here are almost detritus-free, and with the exception of one sample with Al concentration at 0.2 wt.%, all other IFs show Al content <0.1 wt.% (Figure 3). The Fe and Si contents in IFs vary between 31.7 and 63.1 wt.% and between 33.3 and 54.2 wt.%, respectively, indicating that no open system alteration and/or mass loss (e.g., silica leaching) took place after rock deposition. Additionally, these rocks experienced low metamorphic grade (Krymsky et al., 2007; Machado et al., 1991; Rosière et al., 2006), which make them an ideal target to explore past redox conditions in the basin.

Rare earth elements are generally found under a single oxidation state (+3) and share similar geochemical behavior, but two of them, cerium (Ce) and europium (Eu), can behave differently depending on local and/or global redox conditions. Under oxic conditions, Ce can be oxidized from its trivalent to tetravalent state, and less soluble Ce(IV) is readily removed from seawater onto Mn(IV)-Fe(III)-oxyhydroxides, organic matter, and clay particles (Konhauser et al., 2017). This behavior imparts a negative cerium anomaly on modern oxygenated seawater. Most pre-GOE IFs that were not altered by secondary processes (e.g., Bonnand et al., 2020) lack a negative Ce anomaly (e.g., Døssing et al., 2009; Haugaard et al., 2013, Haugaard, Ootes, et al., 2016; Hofmann, 2005; Lindenmayer et al., 2001; Mloszewska et al., 2012; Planavsky et al., 2010) indicating that the adsorption of REY occurred under anoxic water conditions. Similarly, IFs from Carajás show no significant true Ce anomalies, either positive or negative, as indicated by the general absence of data with $Ce/Ce^* < 1$ and $Pr/Pr^* > 1$, or $Ce/Ce^* > 1$ and $Pr/Pr^* < 1$, respectively (Figure 5). We attribute the few values falling in the $Ce/Ce^*<1$ and $Pr/Pr^*>1$ field, close to PAAS values of 1, as reflecting either small compositional differences between PAAS and local detrital inputs, or artifacts arising from the slightly curved REE spectra of our dataset. Calculations of Ce anomalies using alternatively proposed projections (e.g., calculation of Ce^* by projection backward from Pr and Nd; Lawrence and Kamber, 2006) yielded non-negligible but clearly false Ce anomalies that are most likely explained by the same potential artifacts; the Bau and Dulski (1996) method proved more reliable in this regard as the Ce anomalies are clearly identified as artifacts. A comparison with Archean IFs from Isua, Greenland, demonstrates similar anoxic conditions, in contrast to modern microbialites and seawater that show the clear imprint of Ce redox cycling in an oxygenated environment (Figure 5). Additionally, Paleoproterozoic IFs from other cratons throughout the globe argue in favor of more oxidizing conditions with Ce/Ce^* values <0.9 and $Pr/Pr^*>1.02$, contrasting with Archean and Neoarchean values (Oonk et al., 2018; Sampaio et al., 2018; Wang et al., 2016; Warchola et al., 2018). This suggests that the Carajás IFs are formed under anoxic conditions, also suggested by previous studies in the basin (Justo et al., 2020), possibly due to limited generation and accumulation of O_2 produced by oxygenic photosynthetic organisms (if present) that were not likely abundant during the Late Archean (Ossa et al., 2019).

Europium can be reduced to a divalent state under high-temperature and low-Eh conditions, rendering it more soluble under hydrothermal conditions than strictly trivalent REYs (Bau & Möller, 1993). Consequently, hydrothermal fluids from modern and past environments are characterized by a positive Eu anomaly, a feature usually interpreted as a hydrothermal Fe source in IFs. A compilation of Eu anomalies and their variation in time are shown for the major known IFs (Figure 6). A significant increase in the magnitude of positive Eu anomalies was already noted for IFs deposited from ~2.7 to 2.6 Ga (Viehmann et al., 2015). Here, we report unprecedented positive anomalies for the ~2.74 Ga Carajás IFs, with Eu/Eu^* values up to 18 (Figure 6), as compared to maximum values of ~8 and ~5 from other Neoarchean IFs (Garcia et al., 2016; Viehmann, Bau, Hoffmann, et al., 2015). Moreover, the fact that there is no depletion in LREY compared with HREY in our samples (average Pr/Yb_{sn} value of 1.06), which is normally found in modern seawater and reflected

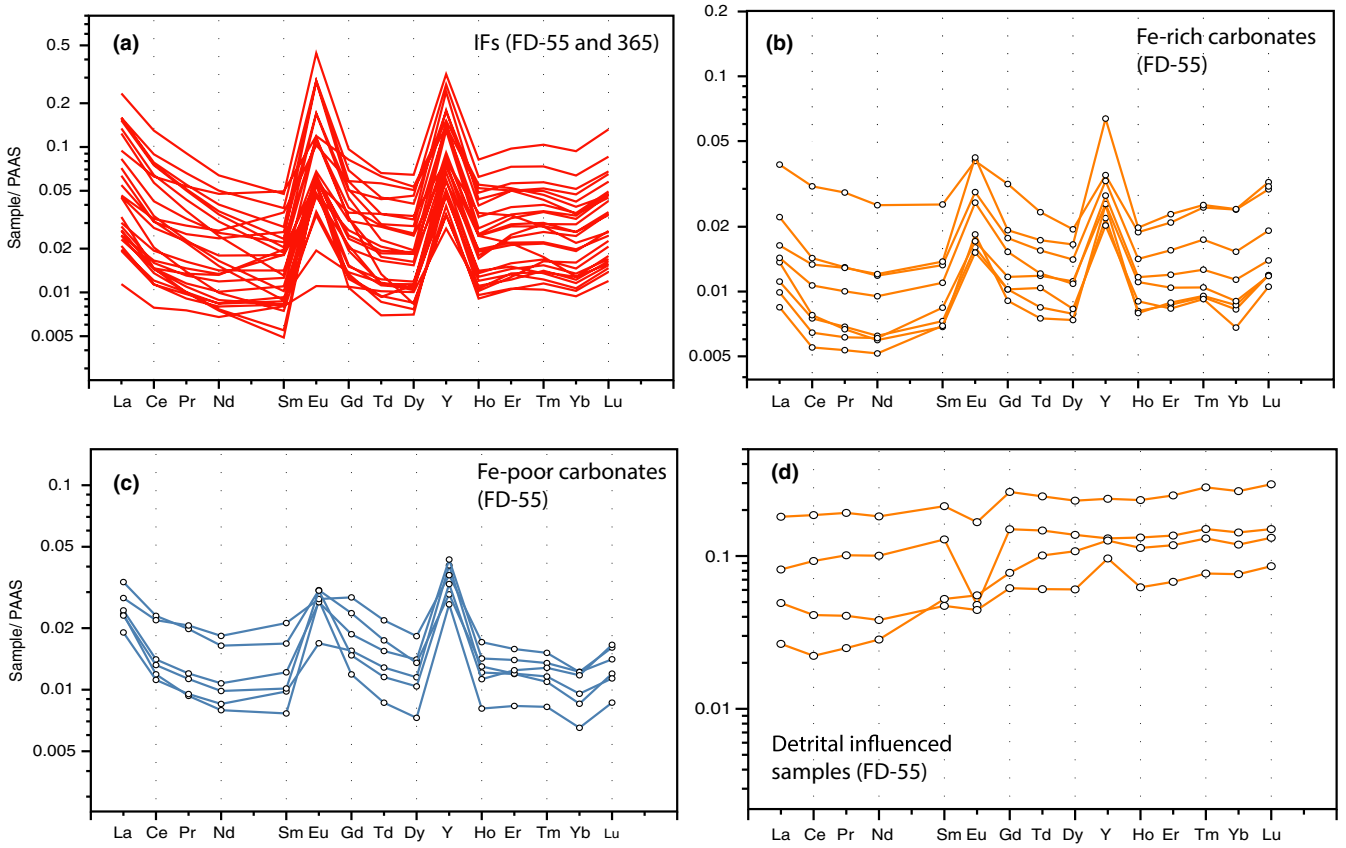

FIGURE 4 Rare earth element and yttrium (REY) abundances normalized to Post-Archean Australian Shales (PAAS) for IFs, Fe-rich, and Fe-poor carbonates (a–c), including few samples influenced by detrital contamination (d)

in a Pr/Yb_{sn} ratio < 1 (e.g., Bolhar et al., 2004), reinforces the idea that the REY signatures in Carajás IFs reflect the mixing of seawater and hydrothermal fluids. This suggests that IF deposition in the Carajás Basin coincided with a period of intense hydrothermal activity, possibly triggered by a major mantle plume event (Viehmann, Bau, Hoffmann, et al., 2015). The Carajás Basin is so far the only location that has recorded such strong positive Eu anomaly, which can be related to a combination of factors, such as IF deposition in a restricted environment where significant hydrothermal activity was taking place. This differs from previous studied Neoarchean and Paleoproterozoic IFs that likely had a more pronounced contribution from open ocean seawater (Viehmann, Bau, Hoffmann, et al., 2015). This intense hydrothermal activity would have provided substantial ferrous iron and maintained general anoxic conditions in the Carajás Basin.

5.2 | Defining an oxidative mechanism from Fe and C isotopes

The presence of ferric minerals in IFs requires oxidation of $Fe(II)_{aq}$ to $Fe(III)_{aq}$ leading to subsequent precipitation of Fe-oxyhydroxide particles (Tangalos et al., 2010). Under oxic conditions and at circum-neutral pH, $Fe(II)_{aq}$ can be rapidly and completely oxidized to thermodynamically stable $Fe(III)_{aq}$ without significant Fe isotope fractionation; thus, Fe(III) oxyhydroxides will inherit the Fe isotopic composition of the Fe(II) source (Rouxel et al., 2018). However, if oxidation rates are slow, such as under low-Eh conditions, Fe(II) can be partially oxidized, producing large Fe isotope fractionation between Fe(II) and Fe(III) species and a ferric iron precipitate enriched in heavy isotopes, as observed in many Archean IFs (Czaja et al., 2013, 2018; Dauphas, Van, et al., 2004; Planavsky et al., 2012). Very low degrees of partial oxidation yield ferric iron precipitates with the largest heavy isotope enrichments, with fractionation also theoretically increasing with decreasing temperature (Anbar et al., 2005). Additionally, sample alteration by metamorphism was shown as an unlikely process to explain heavy δ^{56}Fe values, thus reflecting changes in the biogeochemical cycle of Fe (Dauphas et al., 2007; Frost et al., 2007; Hyslop et al., 2008). The Fe isotope composition of the 2.74 Ga IFs in the Carajás Basin is enriched in heavy isotopes but also remarkably homogeneous, with an average δ^{56}Fe value of +1.39 ± 0.22‰ (1SD, n = 27; Figure 7). Assuming hydrothermally sourced $Fe(II)_{aq}$ remained similar in isotopic composition throughout Earth's history, with δ^{56}Fe values close to modern hydrothermal vent systems (e.g.,~−0.5 to 0‰, Heard & Dauphas, 2020), our positive Fe isotope data support dissolved Fe content in excess of available oxidizing agents in the Carajás Basin since low degrees of partial Fe oxidation can be deduced in both cores from Serra Sul and Serra Norte,

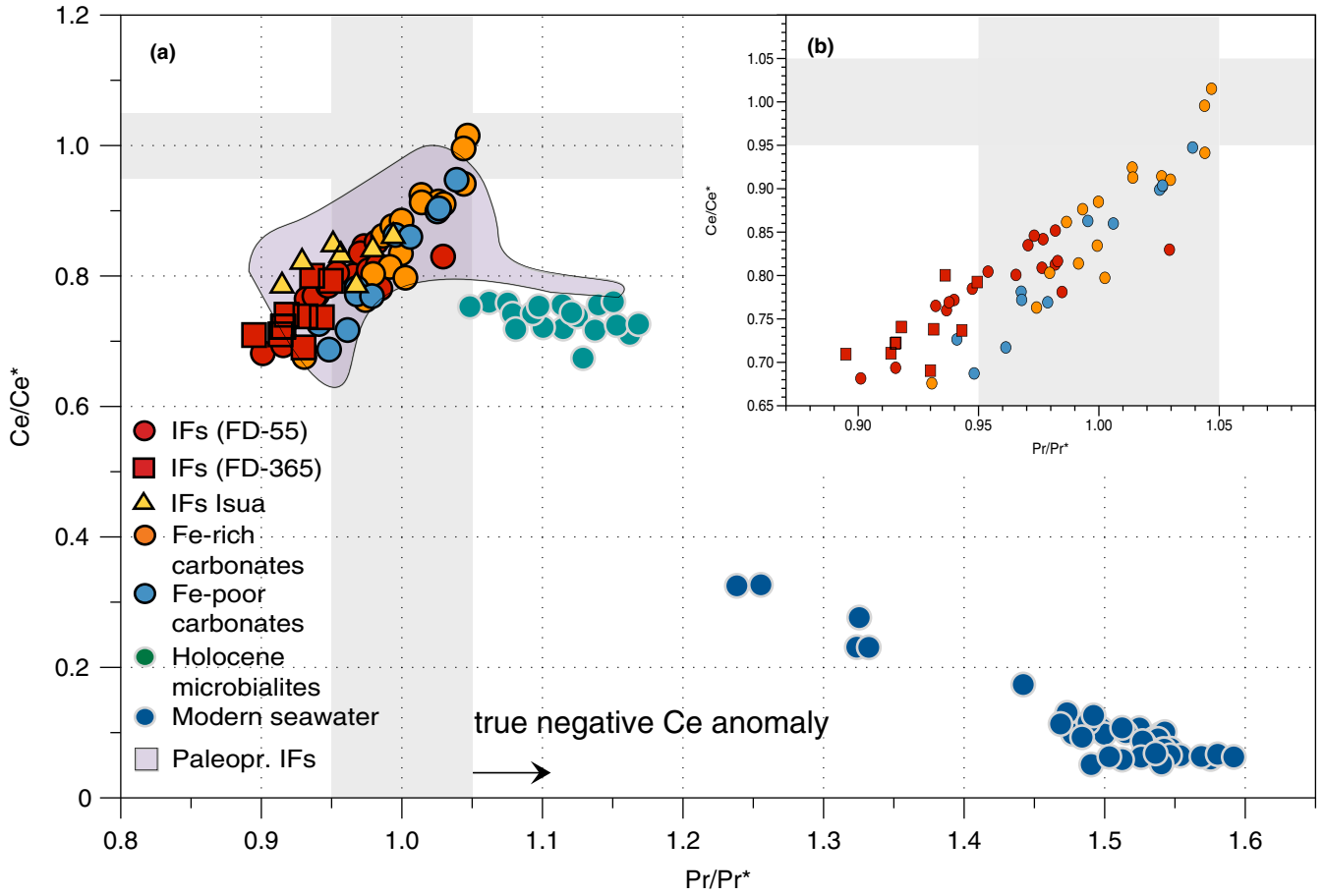

FIGURE 5 Ce anomalies in IFs and carbonates from the CMP compared with IFs from Isua, Greenland (Bolhar et al., 2004), Paleoproterozoic IFs (Bau & Dulski, 1996; Frei et al., 2008; Haugaard et al., 2016; Oonk et al., 2018; Teixeira et al., 2017) Holocene microbialites (Webb & Kamber, 2000), and modern seawater (Zhang & Nozaki, 1996; a), and detailed view of the studied sample set (b)

which are located 50 km from each other. Additionally, the δ^{56}Fe values between −0.4 and +0.07‰ of Fe-poor carbonates in core FD55 further corroborate a fluid source around 0‰ since Fe isotope fractionation between Fe-carbonate and $Fe(II)_{aq}$ ranges between −0.2 and −0.7‰ (Blanchard et al., 2009; Wiesli et al., 2004). The homogeneity of δ^{56}Fe values of IFs within each core and between the two cores can only be explained by a constant and well-buffered Fe isotope composition of seawater at the basin scale. This implies a constant rejuvenation of Fe(II) from the source into the water column, as opposed to a limited source that would result in a depleted δ^{56}Fe eventually recorded in the sediment. In this case, an isotopically light residual iron was not expressed, but likely sequestered in carbonates and pyrites. This suggests that dissolved Fe(II) concentrations were high and little affected by Fe-oxyhydroxide precipitation, again supporting strong hydrothermal activity in the basin, in agreement with the prominent Eu anomaly. The homogeneity of δ^{56}Fe values in IFs indicates a constancy in both δ^{56}Fe values of the dissolved Fe(II) source and the magnitude of the isotope fractionation leading to the formation of Fe precipitate.

The oxidizing mechanism involved in this partial oxidation can be difficult to define based solely on Fe isotopes. According to most models regarding IF genesis, either anoxygenic or oxygenic photosynthesis is the main responsible mechanism, discarding previous models that invoke the reduced Fe-silicate phase (e.g., greenalite) as a primary precipitate (Robbins, Funk, et al., 2019; Tosca et al., 2016). Photo-oxidation by UV photons is proven to be an effective abiotic mechanism to oxidize Fe(II) to Fe(III) with experimental results showing a product enriched in the heavy Fe isotope, consistent with measured values in IFs (Nie et al., 2017). However, previous studies have demonstrated as an unlikely mechanism for extensive IF deposition during the Archean (Konhauser et al., 2007; Pecoits et al., 2015). Based on REY systematics and Fe isotopes, anoxic conditions likely prevailed during IF deposition in the Carajás Basin; thus, anoxygenic photosynthesis would appear to be the most plausible oxidizing mechanism. Experimental studies estimated Fe isotope fractionation of +2.3 ± 0.3‰ for Fe(II) oxidation by photoferrotrophs in conditions similar to Precambrian oceans (Wu et al., 2017). A related experiment with the same bacterial strain, however in the absence of Si, provided a δ^{56}Fe fractionation between Fe(III) precipitates and aqueous Fe(II) ranging from +0.96‰ to +1.98‰ (Swanner, Wu, et al., 2015), while a freshwater bacterial strain showed Fe isotope fractionation of ~+1.5 ± 0.2‰ (Croal et al., 2004). The remarkable

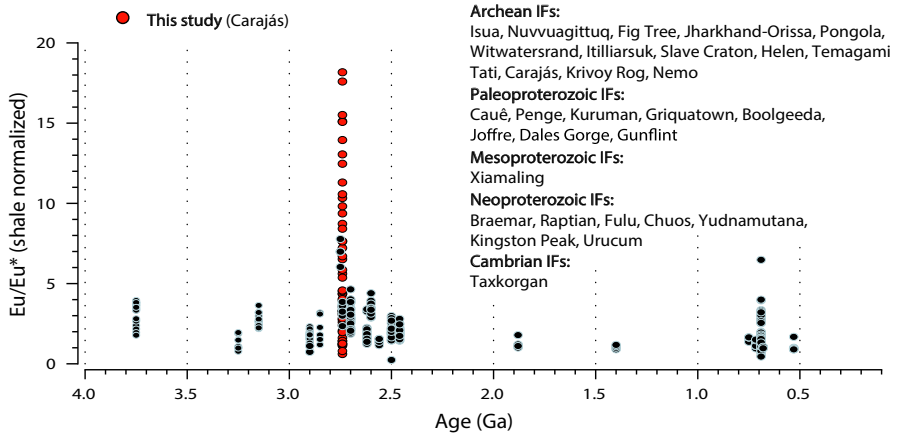

FIGURE 6 Compilation of shale-normalized Eu anomalies for major IFs deposited mainly throughout the Precambrian, including Archean (Alexander et al., 2008; Bau & Alexander, 2009; Bhattacharya et al., 2007; Derry & Jacobsen, 1990; Døssing et al., 2009; Fabre et al., 2011; Frei et al., 2008; Frei & Polat, 2007; Garcia et al., 2016; Haugaard et al., Ootes, 2016; Haugaard, Pecoits, et al., 2016; Haugaard et al., 2013, 2017; Hofmann, 2005; Mloszewska et al., 2012; Viehmann, Bau, Hoffmann, et al., 2015; Viehmann, Bau, Smith, et al., 2015), Paleoproterozoic (Bau & Dulski, 1996; Danielson et al., 1992; Lantink et al., 2018; Teixeira et al., 2017; Warchola et al., 2018), Mesoproterozoic (Canfield et al., 2018), Neoproterozoic (Busigny et al., 2018; Halverson et al., 2011; Lechte et al., 2019; Lottermoser & Ashley, 2000; Viehmann et al., 2016), and Cambrian IFs (Li et al., 2018)

FIGURE 7 Iron isotope fractionation factors of IFs and carbonates (this study) including previous results from the Carajás Basin (Fabre et al., 2011) compared with experimental studies showing fractionation factors for different oxidizing mechanisms (Bullen et al., 2001; Croal et al., 2004; Nie et al., 2017; Wu et al., 2012), inorganic mineral precipitation (Frierdich et al., 2014, 2019; Wiesli et al., 2004), and dissimilatory iron reduction (DIR; Crosby et al., 2007; Johnson et al., 2005)

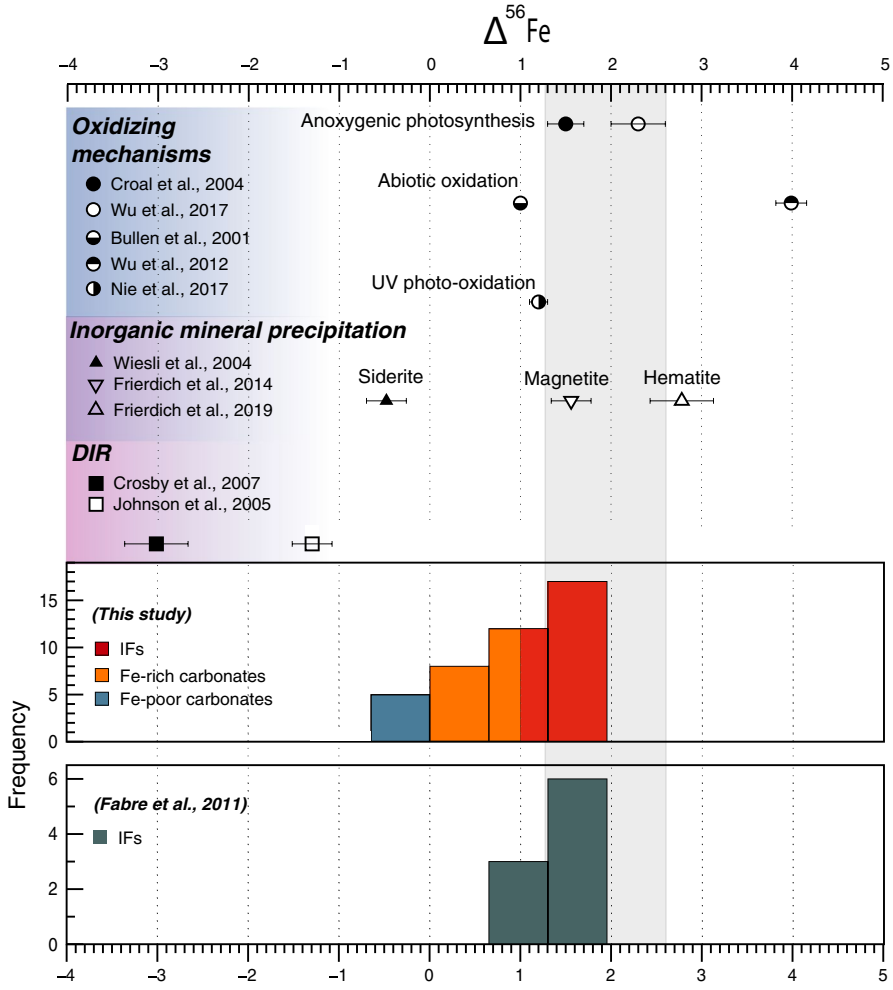

homogeneous δ^{56}Fe values (~+1.39‰) of Carajás IFs imply that the isotope fractionation associated with Fe oxidation was constant both in time and in space. Although the Fe isotope composition of seawater at that time is unknown, a value between −0.5 and 0‰ seems reasonable (Heard & Dauphas, 2020; Johnson et al., 2008), which yields an overall Fe isotope fractionation between fluid and

Fe-oxyhydroxide comprised between +1.35 and 1.85‰. These fractionation values determined from the Fe isotope compositions measured in the present study and previous data obtained on the Carajás Basin (e.g., Fabre et al., 2011) are consistent with the range inferred from experimental studies described above, further supporting photoferrotrophic bacteria as a potential oxidizing pathway (Figure 7). Additionally, variations in the carbon isotope composition of sedimentary organic matter provide further insights into diverse mechanisms used by organisms to fix organic matter (Hayes, 2001). Carbon isotope ratios in the studied IFs and carbonates show variable $\delta^{13}C_{org}$ values, ranging from −23.50 to −28.17‰ and −21.17 to −31.80‰, respectively (Figure 8). The average $\delta^{13}C_{org}$ value of −25.6 ± 1.7‰ ($n = 5$) in IFs is consistent with a kinetic isotope fractionation produced by autotrophic organisms, which are depleted in ^{13}C compared with the CO_2 source (Schidlowski, 2001). Moreover, the organic carbon content in the IFs from Carajás, which varies from 0.01 to 0.06 wt.%, is consistent with previous published values (Thompson et al., 2019). Given the range of both $\delta^{13}C_{org}$ and $\delta^{56}Fe$ values, and considering that Fe(II) was likely dissolved in excess as opposed to available oxidizing agents, we cannot completely rule out an operating cryptic oxygen cycle. This suggests that chemolithoautotrophic and/or microaerophilic organisms could have been thriving under limited oxygen conditions (Konhauser et al., 2002; Smith et al., 2013). Overall, our results argue for autotrophic photosynthesis as the main mechanism of primary production in the Carajás Basin, which, together with REY and Fe isotope data, more likely support the anoxygenic photosynthesis hypothesis.

The role of photoferrotrophs in the Archean is considered to be significant, as these organisms have been suggested to account for most, if not all, Fe(III) deposited in IFs (Konhauser et al., 2002, 2018; Schad et al., 2019). Ferruginous conditions might have been toxic for cyanobacteria in early Precambrian oceans (e.g., Swanner, Mloszewska, et al., 2015), but we cannot completely rule out their presence in surface oxic layers where Fe(II) concentrations might be suppressed. In any case, photoferrotrophs could have oxidized dissolved hydrothermal Fe(II) before reaching the surface (e.g., Kappler et al., 2005; Ozaki et al., 2019) as they are more adapted to low-light conditions (Jones et al., 2015). The ecophysiology of photoferrotrophs likely favored their abundance in Precambrian oceans (Hegler et al., 2008; Posth et al., 2008) as modern analogs have provided palpable evidence of their role in Fe cycling, particularly as agents of Fe oxidation (Koeksoy et al., 2016; Llirós et al., 2015; Walter et al., 2014). Previous studies usually refer to photosynthesis, directly or indirectly, as the main oxidizing mechanism forming Fe(III) minerals in IFs (e.g., Croal et al., 2009; Johnston et al., 2009; Czaja et al., 2013, 2018; Gauger et al., 2015; Gauger et al., 2016; Thompson et al., 2019). However, by combining trace element data with Fe and C isotopes, we propose anoxygenic photosynthesis as a predominant oxidizing mechanism favoring IF deposition in the Carajás Basin.

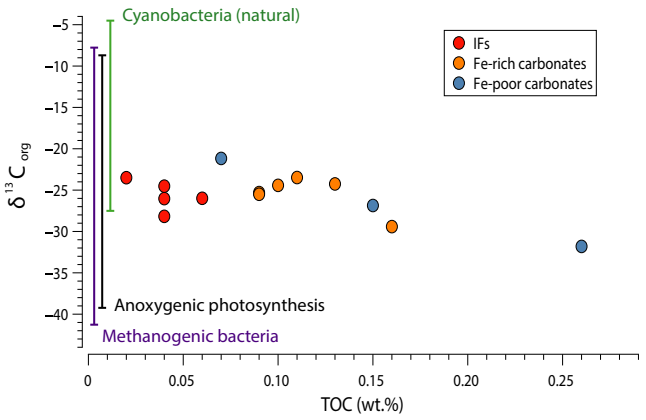

FIGURE 8 Distribution of organic carbon isotope compositions from IFs and carbonates, including ranges characterizing cyanobacteria, methanogenic bacteria, and anoxygenic photosynthetic bacteria (Schidlowski, 2001)

6 | CONCLUSIONS

The approach used here combines REY data with Fe and C isotopes to provide evidence that photoferrotrophs were active in the Carajás Basin and were oxidizing Fe coupled to the fixation of carbon using light energy, without the need of free oxygen (Kappler & Newman, 2004). Despite the indication of oxygenic photosynthesis during the Archean in oceanic and terrestrial settings (e.g., Planavsky et al., 2014; Lalonde & Konhauser, 2015; Eickmann et al., 2018), the Carajás IFs show consistent and narrow positive range in $\delta^{56}Fe$ values, which can be best explained by partial Fe oxidation in conditions with very low to no free O_2, while Fe-rich and Fe-poor carbonates precipitated restrictedly in potentially less reducing conditions. Moreover, a constant and significant hydrothermal Fe(II) source, shown by the highest Eu anomalies registered in IFs, avoided the depletion of an Fe(II) reservoir, as opposed to later Paleoproterozoic IFs in the Hamersley and Transvaal basins (Czaja et al., 2018). Thus, we infer that photoferrotrophic bacteria were responsible for the main iron oxidation mechanism via anoxygenic photosynthesis, as suggested by $\delta^{13}C_{org}$ values, that led to the precipitation of ferric minerals and subsequent deposition of IFs at a regional scale in the Carajás basin.

ACKNOWLEDGMENTS

This research was funded by Fundação de Amparo à Pesquisa do Estado de São Paulo, FAPESP (2019/16271-0; 2018/05892-0; 2015/16235-2; 2018/02645-2; 2019/16066-7). We thank Pascale Louvat, Bleuenn Guéguen, and Céline Liorzou for their technical assistance during MC-ICP-MS, HR-ICP-MS, and ICP-AES analyses. We also like to thank Subject Editor Andreas Kappler, Sean Crowe, and three anonymous reviewers for their comments and suggestions that greatly improved this manuscript.

DATA AVAILABILITY STATEMENT

The data that supports the findings of this study are available in the supplementary material of this article.

ORCID

Eric Siciliano Rego https://orcid.org/0000-0002-6590-5332
Vincent Busigny https://orcid.org/0000-0001-7556-0772
Amaury Bouyon https://orcid.org/0000-0002-1088-6269
Camille Rossignol https://orcid.org/0000-0003-0082-4854
Marly Babinski https://orcid.org/0000-0003-2444-2404

REFERENCES

Alexander, B. W., Bau, M., Andersson, P., & Dulski, P. (2008). Continentally-derived solutes in shallow Archean seawater: Rare earth element and Nd isotope evidence in iron formation from the 2.9 Ga Pongola Supergroup, South Africa. *Geochimica et Cosmochimica Acta*, *72*, 378–394. https://doi.org/10.1016/j.gca.2007.10.028

Anbar, A. D., Jarzecki, A. A., & Spiro, T. G. (2005). Theoretical investigation of iron isotope fractionation between Fe(H2O)63+ and Fe(H2O)62+: Implications for iron stable isotope geochemistry. *Geochimica et Cosmochimica Acta*, *69*, 825–837. https://doi.org/10.1016/j.gca.2004.06.012

Bau, M., & Alexander, B. W. (2009). Distribution of high field strength elements (Y, Zr, REE, Hf, Ta, Th, U) in adjacent magnetite and chert bands and in reference standards FeR-3 and FeR-4 from the Temagami iron-formation, Canada, and the redox level of the Neoarchean ocean. *Precambrian Research*, *174*, 337–346. https://doi.org/10.1016/j.precamres.2009.08.007

Bau, M., & Dulski, P. (1996). Distribution of yttrium and rare-earth elements in the Penge and Kuruman iron-formations, Transvaal Supergroup, South Africa. *Precambrian Research*, *79*, 37–55. https://doi.org/10.1016/0301-9268(95)00087-9

Bau, M., & Möller, P. (1993). Rare earth element systematics of the chemically precipitated component in early precambrian iron formations and the evolution of the terrestrial atmosphere-hydrosphere-lithosphere system. *Geochimica et Cosmochimica Acta*, *57*, 2239–2249. https://doi.org/10.1016/0016-7037(93)90566-F

Beisiegel, V. D. R., Bernardelli, A. L., Drummond, N. F., Ruff, A. W., & Tremaine, J. W. R. (1973). Geologia e Recursos Minerais da Serra dos Carajás. *Revista Brasileira de Geociências*, *3*, 215–242. https://doi.org/10.25249/0375-7536.1973215242

Bhattacharya, H. N., Chakraborty, I., & Ghosh, K. K. (2007). Geochemistry of some banded iron-formations of the Archean supracrustals, Jharkhand-Orissa region, India. *Journal of Earth System Science*, *116*, 245–259. https://doi.org/10.1007/s12040-007-0024-4

Blanchard, M., Poitrasson, F., Méheut, M., Lazzeri, M., Mauri, F., & Balan, E. (2009). Iron isotope fractionation between pyrite (FeS2), hematite (Fe2O3) and siderite (FeCO3): A first-principles density functional theory study. *Geochimica et Cosmochimica Acta*, *73*, 6565–6578. https://doi.org/10.1016/j.gca.2009.07.034

Blankenship, R. E., Sadekar, S., & Rymond, J. (2007). The evolutionary transition from anoxygenic to oxygenic photosynthesis. In P. G. Falkowski & A. H. Knoll (Eds.), *Evolution of Primary Producers in the Sea* (pp. 21–35). Elsevier.

Bolhar, R., Kamber, B. S., Moorbath, S., Fedo, C. M., & Whitehouse, M. J. (2004). Characterisation of early Archaean chemical sediments by trace element signatures. *Earth and Planetary Science Letters*, *222*, 43–60. https://doi.org/10.1016/j.epsl.2004.02.016

Bonnand, P., Lalonde, S. V., Boyet, M., Heubeck, C., Homann, M., Nonnotte, P., Foster, I., Konhauser, K. O., & Köhler, I. (2020). Post-depositional REE mobility in a Paleoarchean banded iron formation revealed by La-Ce geochronology: A cautionary tale for signals of ancient oxygenation. *Earth and Planetary Science Letters*, *547*, 116452. https://doi.org/10.1016/j.epsl.2020.116452

Bullen, T. D., White, A. F., Childs, C. W., Vivit, D. V., & Schultz, M. S. (2001). Demonstration of significant abiotic iron isotope fractionation in nature. *Geology*, *29*, 699–702. https://doi.org/10.1130/0091-7613(2001)029<0699:DOSAII>2.0.CO;2

Busigny, V., Planavsky, N. J., Goldbaum, E., Lechte, M. A., Feng, L., & Lyons, T. W. (2018). Origin of the Neoproterozoic Fulu iron formation, South China: Insights from iron isotopes and rare earth element patterns. *Geochimica et Cosmochimica Acta*, *242*, 123–142. https://doi.org/10.1016/j.gca.2018.09.006

Busigny, V., Planavsky, N. J., Jézéquel, D., Crowe, S., Louvat, P., Moureau, J., Viollier, E., & Lyons, T. W. (2014). Iron isotopes in an Archean ocean analogue. *Geochimica et Cosmochimica Acta*, *133*, 443–462. https://doi.org/10.1016/j.gca.2014.03.004

Cabral, A. R., Bühn, B., Seabra Gomes, A. A., Galbiatti, H. F., Lehmann, B., & Halder, S. (2017). Multiple sulfur isotopes from the Neoarchaean Serra Sul black shale, Carajás mineral province, northern Brazil. *Journal of South American Earth Sciences*, *79*, 377–383. https://doi.org/10.1016/j.jsames.2017.08.002

Cabral, A. R., Creaser, R. A., Nägler, T., Lehmann, B., Voegelin, A. R., Belyatsky, B., Pašava, J., Seabra Gomes, A. A., Galbiatti, H., Böttcher, M. E., & Escher, P. (2013). Trace-element and multi-isotope geochemistry of Late-Archean black shales in the Carajás iron-ore district, Brazil. *Chemical Geology*, *362*, 91–104. https://doi.org/10.1016/j.chemgeo.2013.08.041

Canfield, D. E., Habicht, K. S., & Thamdrup, B. (2000). The Archean sulfur cycle and the early history of atmospheric oxygen. *Science*, *288*, 658–661. https://doi.org/10.1126/science.288.5466.658

Canfield, D. E., Rosing, M. T., & Bjerrum, C. (2006). Early anaerobic metabolisms. *Philosophical Transactions of the Royal Society B: Biological Sciences*, *361*, 1819–1834. https://doi.org/10.1098/rstb.2006.1906

Canfield, D. E., Zhang, S., Wang, H., Wang, X., Zhao, W., Su, J., Bjerrum, C. J., Haxen, E. R., & Hammarlund, E. U. (2018). A Mesoproterozoic iron formation. *Proceedings of the National Academy of Sciences of the United States of America*, *115*, E3895–E3904. https://doi.org/10.1073/pnas.1720529115

Cheng, C., Busigny, V., Ader, M., Thomazo, C., Chaduteau, C., & Philippot, P. (2019). Nitrogen isotope evidence for stepwise oxygenation of the ocean during the Great Oxidation Event. *Geochimica et Cosmochimica Acta*, *261*, 224–247. https://doi.org/10.1016/j.gca.2019.07.011

Cotten, J., Le, D. A., Bau, M., Caroff, M., Maury, R. C., Dulski, P., Fourcade, S., Bohn, M., & Brousse, R. (1995). Origin of anomalous rare-earth element and yttrium enrichments in subaerially exposed basalts: Evidence from French Polynesia. *Chemical Geology*, *119*, 115–138. https://doi.org/10.1016/0009-2541(94)00102-E

Craddock, P. R., & Dauphas, N. (2011). Iron isotopic compositions of geological reference materials and chondrites. *Geostandards and Geoanalytical Research*, *35*, 101–123. https://doi.org/10.1111/j.1751-908X.2010.00085.x

Croal, L. R., Jiao, Y., Kappler, A., & Newman, D. K. (2009). Phototrophic Fe(II) oxidation in an atmosphere of H2: Implications for Archean banded iron formations. *Geobiology*, *7*, 21–24.

Croal, L. R., Johnson, C. M., Beard, B. L., & Newman, D. K. (2004). Iron isotope fractionation by Fe(II)-oxidizing photoautotrophic bacteria. *Geochimica et Cosmochimica Acta*, *68*, 1227–1242.

Crosby, H. A., Roden, E. E., Johnson, C. M., & Beard, B. L. (2007). The mechanisms of iron isotope fractionation produced during dissimilatory Fe(III) reduction by Shewanella putrefaciens and Geobacter sulfurreducens. *Geobiology*, *5*, 169–189. https://doi.org/10.1111/j.1472-4669.2007.00103.x

Crowe, S. A., Jones, C. A., Katsev, S., Magen, C., O'Neill, A. H., Sturm, A., Canfield, D. E., Haffner, G. D., Mucci, A., Sundby, B., & Fowle, D. A. (2008). Photoferrotrophs thrive in an Archean Ocean analogue. *Proceedings of the National Academy of Sciences of the United States of America*, *105*, 15938–15943. https://doi.org/10.1073/pnas.0805313105

Czaja, A. D., Johnson, C. M., Beard, B. L., Roden, E. E., Li, W., & Moorbath, S. (2013). Biological Fe oxidation controlled deposition of banded

iron formation in the ca. 3770Ma Isua Supracrustal Belt (West Greenland). *Earth and Planetary Science Letters*, *363*, 192–203. https://doi.org/10.1016/j.epsl.2012.12.025

Czaja, A. D., Van, K. M. J., Beard, B. L., & Johnson, C. M. (2018). A multistage origin for Neoarchean layered hematite-magnetite iron formation from the Weld Range, Yilgarn Craton, Western Australia. *Chemical Geology*, *488*, 125–137. https://doi.org/10.1016/j.chemgeo.2018.04.019

Dalstra, H., & Guedes, S. (2004). Giant hydrothermal hematite deposits with Mg-Fe metasomatism: A comparison of the Carajás, Hamersley, and other iron ores. *Economic Geology*, *99*, 1793–1800.

Danielson, A., Möller, P., & Dulski, P. (1992). The europium anomalies in banded iron formations and the thermal history of the oceanic crust. *Chemical Geology*, *97*, 89–100. https://doi.org/10.1016/0009-2541(92)90137-T

Dauphas, N., Janney, P. E., Mendybaev, R. A., Wadhwa, M., Richter, F. M., Davis, A. M., Van, Z. M., Hines, R., & Foley, C. N. (2004). Chromatographic separation and multicollection-ICPMS analysis of iron. Investigating mass-dependent and -independent isotope effects. *Analytical Chemistry*, *76*, 5855–5863.

Dauphas, N., Pourmand, A., & Teng, F. Z. (2009). Routine isotopic analysis of iron by HR-MC-ICPMS: How precise and how accurate? *Chemical Geology*, *267*, 175–184.

Dauphas, N., Van, Z. M., Wadhwa, M., Davis, A. M., Marty, B., & Janney, P. E. (2004). Clues from Fe isotope variations on the origin of early Archean BIFs from Greenland. *Science*, *306*, 2077–2080.

Dauphas, N., van Zuilen, M., Busigny, V., Lepland, A., Wadhwa, M., & Janney, P. E. (2007). Iron isotope, major and trace element characterization of early Archean supracrustal rocks from SW Greenland: Protolith identification and metamorphic overprint. *Geochimica et Cosmochimica Acta*, *71*, 4745–4770.

Derry, L. A., & Jacobsen, S. B. (1990). The chemical evolution of Precambrian seawater: Evidence from REEs in banded iron formations. *Geochimica et Cosmochimica Acta*, *54*, 2965–2977.

Døssing, L. N., Frei, R., Stendal, H., & Mapeo, R. B. M. (2009). Characterization of enriched lithospheric mantle components in ~2.7 Ga Banded Iron Formations: An example from the Tati Greenstone Belt, Northeastern Botswana. *Precambrian Research*, *172*, 334–356.

Eickmann B., Hofmann A., Wille M., Bui T. H., Wing B. A., & Schoenberg R. (2018). Isotopic evidence for oxygenated Mesoarchaean shallow oceans. *Nature Geoscience*, *11*(2), 133–138. https://doi.org/10.1038/s41561-017-0036-x

Fabre, S., Nédélec, A., Poitrasson, F., Strauss, H., Thomazo, C., & Nogueira, A. (2011). Iron and sulphur isotopes from the Carajás mining province (Pará, Brazil): Implications for the oxidation of the ocean and the atmosphere across the Archaean – Proterozoic transition. *Chemical Geology*, *289*, 124–139.

Farquhar, J., Bao, H., & Thiemens, M. (2000). Atmospheric influence of Earth's earliest sulfur cycle. *Science*, *289*, 756–758.

Fischer, W. W., Hemp, J., & Johnson, J. E. (2016). Evolution of oxygenic photosynthesis. *Annual Review of Earth and Planetary Sciences*, *44*, 647–683.

Frei, R., Dahl, P. S., Duke, E. F., Frei, K. M., Hansen, T. R., Frandsson, M. M., & Jensen, L. A. (2008). Trace element and isotopic characterization of Neoarchean and Paleoproterozoic iron formations in the Black Hills (South Dakota, USA): Assessment of chemical change during 2.9-1.9 Ga deposition bracketing the 2.4-2.2 Ga first rise of atmospheric oxygen. *Precambrian Research*, *162*, 441–474.

Frei, R., & Polat, A. (2007). Source heterogeneity for the major components of ~ 3.7 Ga Banded Iron Formations (Isua Greenstone Belt, Western Greenland): Tracing the nature of interacting water masses in BIF formation. *Earth and Planetary Science Letters*, *253*, 266–281. https://doi.org/10.1016/j.epsl.2006.10.033

Frierdich, A. J., Beard, B. L., Scherer, M. M., & Johnson, C. M. (2014). Determination of the Fe(II)aq-magnetite equilibrium iron isotope fractionation factor using the three-isotope method and a multi-direction approach to equilibrium. *Earth and Planetary Science Letters*, *391*, 77–86. https://doi.org/10.1016/j.epsl.2014.01.032

Frierdich, A. J., Nebel, O., Beard, B. L., & Johnson, C. M. (2019). Iron isotope exchange and fractionation between hematite (α-Fe2O3) and aqueous Fe(II): A combined three-isotope and reversal-approach to equilibrium study. *Geochimica et Cosmochimica Acta*, *245*, 207–221. https://doi.org/10.1016/j.gca.2018.10.033

Frost, C. D., von Blanckenburg, F., Schoenberg, R., Frost, B. R., & Swapp, S. M. (2007). Preservation of Fe isotope heterogeneities during diagenesis and metamorphism of banded iron formation. *Contributions to Mineralogy and Petrology*, *153*, 211–235. https://doi.org/10.1007/s00410-006-0141-0

Garcia, T. I., Gorton, M. P., Li, H., Wortmann, U. G., & Spooner, E. T. C. (2016). The geochemistry of the 2.75 Ga-old Helen Iron Formation, Wawa, Ontario – Insights into iron formation deposition from carbon isotopes and rare earth elements. *Precambrian Research*, *275*, 357–368. https://doi.org/10.1016/j.precamres.2016.01.013

Gauger, T., Byrne, J. M., Konhauser, K. O., Obst, M., Crowe, S., & Kappler, A. (2016). Influence of organics and silica on Fe(II) oxidation rates and cell-mineral aggregate formation by the green-sulfur Fe(II)-oxidizing bacterium Chlorobium ferrooxidans KoFox – Implications for Fe(II) oxidation in ancient oceans. *Earth and Planetary Science Letters*, *443*, 81–89. https://doi.org/10.1016/j.epsl.2016.03.022

Gauger, T., Konhauser, K., & Kappler, A. (2015). Protection of phototrophic iron(II)-oxidizing bacteria from UV irradiation by biogenic iron(III) minerals: Implications for early archean banded iron formation. *Geology*, *43*, 1067–1070. https://doi.org/10.1130/G37095.1

Gibbs, A. K., Wirth, K. R., Hirata, W. K., & Olszewski, W. J. (1986). Age and composition of the Grão Pará Group volcanics, serra dos carajás. *Revista Brasileira De Geociências*, *16*, 201–211. https://doi.org/10.25249/0375-7536.1986201211

Halverson, G. P., Poitrasson, F., Hoffman, P. F., Nédélec, A., Montel, J. M., & Kirby, J. (2011). Fe isotope and trace element geochemistry of the Neoproterozoic syn-glacial Rapitan iron formation. *Earth and Planetary Science Letters*, *309*, 100–112. https://doi.org/10.1016/j.epsl.2011.06.021

Hamilton, T. L. (2019). The trouble with oxygen: The ecophysiology of extant phototrophs and implications for the evolution of oxygenic photosynthesis. *Free Radical Biology and Medicine*, *140*, 233–249. https://doi.org/10.1016/j.freeradbiomed.2019.05.003

Haugaard, R., Frei, R., Stendald, H., & Konhauser, K. (2013). Petrology and geochemistry of the ~2.9 Ga Itilliarsuk banded iron formation and associated supracrustal rocks, West Greenland: Source characteristics and depositional environment. *Precambrian Research*, *229*, 150–176.

Haugaard, R., Ootes, L., Creaser, R. A., & Konhauser, K. O. (2016). The nature of Mesoarchaean seawater and continental weathering in 2.85 Ga banded iron formation, Slave craton, NW Canada. *Geochimica et Cosmochimica Acta*, *194*, 34–56.

Haugaard, R., Ootes, L., & Konhauser, K. (2017). Neoarchaean banded iron formation within a ~2620 Ma turbidite-dominated deep-water basin, Slave craton, NW Canada. *Precambrian Research*, *292*, 130–151.

Haugaard, R., Pecoits, E., Lalonde, S., Rouxel, O., & Konhauser, K. (2016). The Joffre banded iron formation, Hamersley Group, Western Australia: Assessing the palaeoenvironment through detailed petrology and chemostratigraphy. *Precambrian Research*, *273*, 12–37.

Hayes, J. M. (2001). Fractionation of the isotopes of carbon and hydrogen in biosynthetic processes. In J. W. Valley & D. R. Cole (Eds.), *Stable Isotope Geochemistry* (pp. 225–278). The Mineralogical Society of America.

Heard, A. W., & Dauphas, N. (2020). Constraints on the coevolution of oxic and sulfidic ocean iron sinks from archean-paleoproterozoic iron isotope records. *Geology*, *48*, 358–362.

Hegler, F., Posth, N. R., Jiang, J., & Kappler, A. (2008). Physiology of phototrophic iron(II)-oxidizing bacteria: Implications for modern and ancient environments. *FEMS Microbiology Ecology*, *66*, 250–260.

Hofmann, A. (2005). The geochemistry of sedimentary rocks from the Fig Tree Group, Barberton greenstone belt: Implications for tectonic, hydrothermal and surface processes during mid-Archaean times. *Precambrian Research*, *143*, 23–49.

Holland, H. D. (2006). The oxygenation of the atmosphere and oceans. *Philosophical Transactions of the Royal Society of London. Series B, Biological Sciences*, *361*, 903–915.

Hyslop, E. V., Valley, J. W., Johnson, C. M., & Beard, B. L. (2008). The effects of metamorphism on O and Fe isotope compositions in the Biwabik Iron Formation, northern Minnesota. *Contributions to Mineralogy and Petrology*, *155*, 313–328.

James, H. L. (1983). Distribution of banded iron-formation in space and time. *Developments in Precambrian Geology*, *6*, 471–490.

Johnson, C. M., Beard, B. L., Klein, C., Beukes, N. J., & Roden, E. E. (2008). Iron isotopes constrain biologic and abiologic processes in banded iron formation genesis. *Geochimica et Cosmochimica Acta*, *72*, 151–169.

Johnson, C. M., Beard, B. L., & Roden, E. E. (2008). The iron isotope fingerprints of redox and biogeochemical cycling in modern and ancient earth. *Annual Review of Earth and Planetary Sciences*, *36*, 457–493.

Johnson, C. M., Roden, E. E., Welch, S. A., & Beard, B. L. (2005). Experimental constraints on Fe isotope fractionation during magnetite and Fe carbonate formation coupled to dissimilatory hydrous ferric oxide reduction. *Geochimica et Cosmochimica Acta*, *69*, 963–993.

Johnston, D. T., Wolfe-Simon, F., Pearson, A., & Knoll, A. H. (2009). Anoxygenic photosynthesis modulated Proterozoic oxygen and sustained Earth's middle age. *Proceedings of the National Academy of Sciences of the United States of America*, *106*, 16925–16929.

Jones, C., Nomosatryo, S., Crowe, S. A., Bjerrum, C. J., & Canfield, D. E. (2015). Iron oxides, divalent cations, silica, and the early earth phosphorus crisis. *Geology*, *43*, 135–138.

Justo, A. P., Dantas, E. L., Bau, M., Freitas-Silva, F. H., Santos, R. V., & Schorscher, J. H. D. (2020). Paleobasinal to band-scale REE + Y distribution in iron formations from Carajás, Amazon Craton, Brazil. *Ore Geology Reviews*, *127*, 103750.

Kappler, A., & Newman, D. K. (2004). Formation of Fe(III)-minerals by Fe(II)-oxidizing photoautotrophic bacteria. *Geochimica et Cosmochimica Acta*, *68*, 1217–1226.

Kappler, A., Pasquero, C., Konhauser, K. O., & Newman, D. K. (2005). Deposition of banded iron formations by anoxygenic phototrophic Fe(II)-oxidizing bacteria. *Geology*, *33*, 865–868.

Klein, C. (2005). Some Precambrian banded iron-formations (BIFs) from around the world: Their age, geologic setting, mineralogy, metamorphism, geochemistry, and origin. *American Mineralogist*, *90*, 1473–1499.

Klein, C., & Ladeira, E. A. (2002). Petrography and geochemistry of the least altered banded iron-formation of the Archean Carajás formation, northern Brazil. *Economic Geology*, *97*, 643–651.

Koeksoy, E., Halama, M., Konhauser, K. O., & Kappler, A. (2016). Using modern ferruginous habitats to interpret Precambrian banded iron formation deposition. *International Journal of Astrobiology*, *15*, 205–217. https://doi.org/10.1017/S1473550415000373

Konhauser, K. O., Amskold, L., Lalonde, S. V., Posth, N. R., Kappler, A., & Anbar, A. (2007). Decoupling photochemical Fe(II) oxidation from shallow-water BIF deposition. *Earth and Planetary Science Letters*, *258*, 87–100. https://doi.org/10.1016/j.epsl.2007.03.026

Konhauser, K. O., Hamade, T., Raiswell, R., Morris, R. C., Ferris, F. G., Southam, G., & Canfield, D. E. (2002). Could bacteria have formed the Precambrian banded iron formations? *Geology*, *30*, 1079–1082. https://doi.org/10.1130/0091-7613(2002)030<1079:CBHFTP>2.0.CO;2

Konhauser, K. O., Planavsky, N. J., Hardisty, D. S., Robbins, L. J., Warchola, T. J., Haugaard, R., Lalonde, S. V., Partin, C. A., Oonk, P. B. H., Tsikos, H., Lyons, T. W., Bekker, A., & Johnson, C. M. (2017). Iron formations: A global record of Neoarchaean to Palaeoproterozoic environmental history. *Earth-Science Reviews*, *172*, 140–177. https://doi.org/10.1016/j.earscirev.2017.06.012

Konhauser, K. O., Robbins, L. J., Alessi, D. S., Flynn, S. L., Gingras, M. K., Martinez, R. E., Kappler, A., Swanner, E. D., Li, Y. L., Crowe, S. A., Planavsky, N. J., Reinhard, C. T., & Lalonde, S. V. (2018). Phytoplankton contributions to the trace-element composition of Precambrian banded iron formations. *Bulletin of the Geological Society of America*, *130*, 941–951. https://doi.org/10.1130/B31648.1

Krymsky, R. S., Macambira, M. J. B., Lafon, J. M., & Estumano, G. S. (2007). Uranium-lead dating method at the Pará-Iso isotope geology laboratory, UFPA, Belém - Brazil. *Anais da Academia Brasileira de Ciencias*, *79*, 115–128. https://doi.org/10.1590/S0001-37652007000100014

Lalonde, S. V., & Konhauser, K. O. (2015). Benthic perspective on Earth's oldest evidence for oxygenic photosynthesis. *Proceedings of the National Academy of Sciences of the United States of America*, *112*, 995–1000. https://doi.org/10.1073/pnas.1415718112

Lantink, M. L., Oonk, P. B. H., Floor, G. H., Tsikos, H., & Mason, P. R. D. (2018). Fe isotopes of a 2.4 Ga hematite-rich IF constrain marine redox conditions around the GOE. *Precambrian Research*, *305*, 218–235. https://doi.org/10.1016/j.precamres.2017.12.025

Lawrence M. G., & Kamber B. S. (2006). The behaviour of the rare earth elements during estuarine mixing—revisited. *Marine Chemistry*, *100*(1-2), 147–161. https://doi.org/10.1016/j.marchem.2005.11.007

Lechte, M. A., Wallace, M. W., van Smeerdijk Hood, A., Li, W., Jiang, G., Halverson, G. P., Asael, D., McColl, S. L., & Planavsky, N. J. (2019). Subglacial meltwater supported aerobic marine habitats during Snowball Earth. *Proceedings of the National Academy of Sciences of the United States of America*, *116*, 25478–25483. https://doi.org/10.1073/pnas.1909165116

Li, Z. Q., Zhang, L. C., Xue, C. J., Zheng, M. T., Zhu, M. T., Robbins, L. J., Slack, J. F., Planavsky, N. J., & Konhauser, K. O. (2018). Earth's youngest banded iron formation implies ferruginous conditions in the Early Cambrian ocean. *Scientific Reports*, *8*, 1–10.

Lindenmayer, Z., Laux, J., & Teixeira, J. (2001). Consideração sobre a origem das formações ferríferas da Formação Carajás, Serra dos Carajás. *Revista Brasileira de Geociências*, *31*, 21–28.

Llirós, M., Garcià-Armisen, T., Darchambeau, F., Morana, C., Triadó-Margarit, X., Inceoɬlu, Ö., Borrego, C. M., Bouillon, S., Servais, P., Borges, A. V., Descy, J. P., Canfield, D. E., & Crowe, S. A. (2015). Pelagic photoferrotrophy and iron cycling in a modern ferruginous basin. *Scientific Reports*, *5*, 1–8. https://doi.org/10.1038/srep13803

Lottermoser, B. G., & Ashley, P. M. (2000). Geochemistry, petrology and origin of Neoproterozoic ironstones in the eastern part of the Adelaide Geosyncline, South Australia. *Precambrian Research*, *101*, 49–67. https://doi.org/10.1016/S0301-9268(99)00098-4

Macambira, J. B., & Schrank, A. (2002). Químio-estratigrafia e evolução dos jaspilitos da Formação Carajás (PA). *Revista Brasileira de Geociências*, *32*, 567–578. https://doi.org/10.25249/0375-7536.2002324567578

Machado, N., Lindenmayer, Z., Krogh, T. E., & Lindenmayer, D. (1991). U-Pb geochronology of Archean magmatism and basement reactivation in the Carajás area, Amazon shield, Brazil. *Precambrian Research*, *49*, 329–354. https://doi.org/10.1016/0301-9268(91)90040-H

Martin, W. F., Bryant, D. A., & Beatty, J. T. (2018). A physiological perspective on the origin and evolution of photosynthesis. *FEMS Microbiology Reviews*, *42*, 205–231. https://doi.org/10.1093/femsre/fux056

Martins, P. L. G., Toledo, C. L. B., Silva, A. M., Chemale, F., Santos, J. O. S., & Assis, L. M. (2017). Neoarchean magmatism in the southeastern Amazonian Craton, Brazil: Petrography, geochemistry and tectonic significance of basalts from the Carajás Basin. *Precambrian Research*, *302*, 340–357. https://doi.org/10.1016/j.precamres.2017.10.013

McLennan, S. M. (1989). Rare earth elements in sedimentary rocks; influence of provenance and sedimentary processes. *Reviews in Mineralogy and Geochemistry*, *21*(1), 169–200.

Mloszewska, A. M., Pecoits, E., Cates, N. L., Mojzsis, S. J., O'Neil, J., Robbins, L. J., & Konhauser, K. O. (2012). The composition of Earth's oldest iron formations: The Nuvvuagittuq Supracrustal Belt (Québec, Canada). *Earth and Planetary Science Letters*, *317–318*, 331–342. https://doi.org/10.1016/j.epsl.2011.11.020

Moreto, C. P. N., Monteiro, L. V. S., Xavier, R. P., Creaser, R. A., DuFrane, S. A., Tassinari, C. C. G., Sato, K., Kemp, A. I. S., & Amaral, W. S. (2015). Neoarchean and paleoproterozoic iron oxide-copper-gold events at the sossego deposit, Carajás Province, Brazil: Re-Os and U-Pb geochronological evidence. *Economic Geology*, *110*, 809–835.

Muller, É., Ader, M., Chaduteau, C., Cartigny, P., Baton, F., & Philippot, P. (2017). The use of chromium reduction in the analysis of organic carbon and inorganic sulfur isotope compositions in Archean rocks. *Chemical Geology*, *457*, 68–74. https://doi.org/10.1016/j.chemgeo.2017.03.014

Nie, N. X., Dauphas, N., & Greenwood, R. C. (2017). Iron and oxygen isotope fractionation during iron UV photo-oxidation: Implications for early Earth and Mars. *Earth and Planetary Science Letters*, *458*, 179–191. https://doi.org/10.1016/j.epsl.2016.10.035

Oonk, P. B. H., Mason, P. R. D., Tsikos, H., & Bau, M. (2018). Fraction-specific rare earth elements enable the reconstruction of primary seawater signatures from iron formations. *Geochimica et Cosmochimica Acta*, *238*, 102–122. https://doi.org/10.1016/j.gca.2018.07.005

Ossa, F. O., Hofmann, A., Spangenberg, J. E., Poulton, S. W., Stüeken, E. E., Schoenberg, R., Eickmann, B., Wille, M., Butler, M., & Bekker, A. (2019). Limited oxygen production in the Mesoarchean ocean. *Proceedings of the National Academy of Sciences of the United States of America*, *116*, 6647–6652. https://doi.org/10.1073/pnas.1818762116

Ozaki, K., Thompson, K. J., Simister, R. L., Crowe, S. A., & Reinhard, C. T. (2019). Anoxygenic photosynthesis and the delayed oxygenation of Earth's atmosphere. *Nature Communications*, *10*, 3026. https://doi.org/10.1038/s41467-019-10872-z

Pecoits, E., Smith, M. L., Catling, D. C., Philippot, P., Kappler, A., & Konhauser, K. O. (2015). Atmospheric hydrogen peroxide and Eoarchean iron formations. *Geobiology*, *13*, 1–14. https://doi.org/10.1111/gbi.12116

Planavsky, N. J., Asael, D., Hofmann, A., Reinhard, C. T., Lalonde, S. V., Knudsen, A., Wang, X., Ossa Ossa, F., Pecoits, E., Smith, A. J. B., Beukes, N. J., Bekker, A., Johnson, T. M., Konhauser, K. O., Lyons, T. W., & Rouxel, O. J. (2014). Evidence for oxygenic photosynthesis half a billion years before the Great Oxidation Event. *Nature Geoscience*, *7*, 283–286. https://doi.org/10.1038/ngeo2122

Planavsky, N., Bekker, A., Rouxel, O. J., Kamber, B., Hofmann, A., Knudsen, A., & Lyons, T. W. (2010). Rare Earth Element and yttrium compositions of Archean and Paleoproterozoic Fe formations revisited: New perspectives on the significance and mechanisms of deposition. *Geochimica et Cosmochimica Acta*, *74*, 6387–6405. https://doi.org/10.1016/j.gca.2010.07.021

Planavsky, N., Rouxel, O. J., Bekker, A., Hofmann, A., Little, C. T. S., & Lyons, T. W. (2012). Iron isotope composition of some Archean and Proterozoic iron formations. *Geochimica et Cosmochimica Acta*, *80*, 158–169. https://doi.org/10.1016/j.gca.2011.12.001

Posth, N. R., Hegler, F., Konhauser, K. O., & Kappler, A. (2008). Alternating Si and Fe deposition caused by temperature fluctuations in Precambrian oceans. *Nature Geoscience*, *1*, 703–708.

Ribeiro da Luz, B., & Crowley, J. K. (2012). Morphological and chemical evidence of stromatolitic deposits in the 2.75Ga Carajás banded iron formation, Brazil. *Earth and Planetary Science Letters*, *355–356*, 60–72.

Robbins, L. J., Funk, S. P., Flynn, S. L., Warchola, T. J., Li, Z., Lalonde, S. V., Rostron, B. J., Smith, A. J. B., Beukes, N. J., de Kock, M. O., Heaman, L. M., Alessi, D. S., & Konhauser, K. O. (2019). Hydrogeological constraints on the formation of Palaeoproterozoic banded iron formations. *Nature Geoscience*, *12*, 558–563.

Robbins, L. J., Konhauser, K. O., Warchola, T. J., Homann, M., Thoby, M., Foster, I., Mloszewska, A. M., Alessi, D. S., & Lalonde, S. V. (2019). A comparison of bulk versus laser ablation trace element analyses in banded iron formations: Insights into the mechanisms leading to compositional variability. *Chemical Geology*, *506*, 197–224.

Rosière, C. A., Baars, F. J., Seoane, J. C. S., Lobato, L. M., da Silva, L. L., de Souza, S. R. C., & Mendes, G. E. (2006). Structure and iron mineralisation of the Carajás Province. *Transactions of the Institutions of Mining and Metallurgy, Section B: Applied Earth Science*, *115*, 126–133.

Rossignol, C., Siciliano Rego, E., Narduzzi, F., Teixeira, L., Ávila, J. N., Silva, M. A. L., Lana, C., & Philippot, P. (2020). Stratigraphy and geochronological constraints of the Serra Sul Formation (Carajás Basin, Amazonian Craton, Brazil). *Precambrian Research*, *351*, 105981.

Rouxel, O. J. (2005). Iron isotope constraints on the archean and paleoproterozoic ocean redox state. *Science*, *307*, 1088–1091.

Rouxel, O., Dobbek, N., Ludden, J., & Fouquet, Y. (2003). Iron isotope fractionation during oceanic crust alteration. *Chemical Geology*, *202*, 155–182.

Rouxel, O., Toner, B., Germain, Y., & Glazer, B. (2018). Geochemical and iron isotopic insights into hydrothermal iron oxyhydroxide deposit formation at Loihi Seamount. *Geochimica et Cosmochimica Acta*, *220*, 449–482.

Sampaio, G. M. S., Pufahl, P. K., Raye, U., Kyser, K. T., Abreu, A. T., Alkmim, A. R., & Nalini, H. A. (2018). Influence of weathering and hydrothermal alteration on the REE and δ56Fe composition of iron formation, Cauê Formation, Iron Quadrangle, Brazil. *Chemical Geology*, *497*, 27–40.

Satkoski, A. M., Beukes, N. J., Li, W., Beard, B. L., & Johnson, C. M. (2015). A redox-stratified ocean 3.2 billion years ago. *Earth and Planetary Science Letters*, *430*, 43–53.

Schad, M., Konhauser, K. O., Sánchez-Baracaldo, P., Kappler, A., & Bryce, C. (2019). How did the evolution of oxygenic photosynthesis influence the temporal and spatial development of the microbial iron cycle on ancient Earth? *Free Radical Biology and Medicine*, *140*, 154–166.

Schidlowski, M. (2001). Carbon isotopes as biogeochemical recorders of life over 3.8 Ga of earth history: Evolution of a concept. *Precambrian Research*, *106*, 117–134.

Schoenberg, R., & Von, B. F. (2005). An assessment of the accuracy of stable Fe isotope ratio measurements on samples with organic and inorganic matrices by high-resolution multicollector ICP-MS. *International Journal of Mass Spectrometry*, *242*, 257–272.

Smith, A. J. B., Beukes, N. J., & Gutzmer, J. (2013). The composition and depositional environments of mesoarchean iron formations of the west rand group of the witwatersrand supergroup, South Africa. *Economic Geology*, *108*, 111–134.

Strelow, F. W. E. (1980). Improved separation of iron from copper and other elements by anion-exchange chromatography on a 4% cross-linked resin with high concentrations of hydrochloric acid. *Talanta*, *27*, 727–732.

Swanner, E. D., Mloszewska, A. M., Cirpka, O. A., Schoenberg, R., Konhauser, K. O., & Kappler, A. (2015). Modulation of oxygen production in Archaean oceans by episodes of Fe(II) toxicity. *Nature Geoscience*, *8*, 126–130.

Swanner, E. D., Wu, W., Schoenberg, R., Byrne, J., Michel, F. M., Pan, Y., & Kappler, A. (2015). Fractionation of Fe isotopes during Fe(II) oxidation by a marine photoferrotroph is controlled by the formation

of organic Fe-complexes and colloidal Fe fractions. *Geochimica et Cosmochimica Acta*, *165*, 44–61.

Tangalos, G. E., Beard, B. L., Johnson, C. M., Alpers, C. N., Shelobolina, E. S., Xu, H., Konishi, H., & Roden, E. E. (2010). Microbial production of isotopically light iron(II) in a modern chemically precipitated sediment and implications for isotopic variations in ancient rocks. *Geobiology*, *8*, 197–208.

Taylor, P. D. P., Maeck, R., & De, B. P. (1992). Determination of the absolute isotopic composition and Atomic Weight of a reference sample of natural iron. *International Journal of Mass Spectrometry and Ion Processes*, *121*, 111–125.

Teixeira, N. L., Caxito, F. A., Rosière, C. A., Pecoits, E., Vieira, L., Frei, R., Sial, A. N., & Poitrasson, F. (2017). Trace elements and isotope geochemistry (C, O, Fe, Cr) of the Cauê iron formation, Quadrilátero Ferrífero, Brazil: Evidence for widespread microbial dissimilatory iron reduction at the Archean/Paleoproterozoic transition. *Precambrian Research*, *298*, 39–55.

Thompson, K. J., Kenward, P. A., Bauer, K. W., Warchola, T., Gauger, T., Martinez, R., Simister, R. L., Michiels, C. C., Llirós, M., Reinhard, C. T., Kappler, A., Konhauser, K. O., & Crowe, S. A. (2019). Photoferrotrophy, deposition of banded iron formations, and methane production in Archean oceans. *Science Advances*, *5*, 1–10.

Thompson, K. J., Simister, R. L., Hahn, A. S., Hallam, S. J., & Crowe, S. A. (2017). Nutrient acquisition and the metabolic potential of photoferrotrophic Chlorobi. *Frontiers in Microbiology*, *8*, 1–16.

Tolbert, G. E., Tremaine, J. W., Melcher, G. C., & Gomes, C. B. (1971). The recently discovered serra dos carajas iron deposits, Northern Brazil. *Economic Geology*, *66*, 985–994.

Tosca, N. J., Guggenheim, S., & Pufahl, P. K. (2016). An authigenic origin for Precambrian greenalite: Implications for iron formation and the chemistry of ancient seawater. *Bulletin of the Geological Society of America*, *128*, 511–530.

Trendall, A. F., Basei, M. A. S., De, L. J. R., & Nelson, D. R. (1998). SHRIMP zircon U-Pb constraints on the age of the Carajas formation, Grao Para Group, Amazon Craton. *Journal of South American Earth Sciences*, *11*, 265–277.

Viehmann, S., Bau, M., Bühn, B., Dantas, E. L., Andrade, F. R. D., & Walde, D. H. G. (2016). Geochemical characterisation of Neoproterozoic marine habitats: Evidence from trace elements and Nd isotopes in the Urucum iron and manganese formations, Brazil. *Precambrian Research*, *282*, 74–96.

Viehmann, S., Bau, M., Hoffmann, J. E., & Münker, C. (2015). Geochemistry of the Krivoy Rog Banded Iron Formation, Ukraine, and the impact of peak episodes of increased global magmatic activity on the trace element composition of Precambrian seawater. *Precambrian Research*, *270*, 165–180.

Viehmann, S., Bau, M., Smith, A. J. B., Beukes, N. J., Dantas, E. L., & Bühn, B. (2015). The reliability of ~2.9 Ga old Witwatersrand banded iron formations (South Africa) as archives for Mesoarchean seawater: Evidence from REE and Nd isotope systematics. *Journal of African Earth Sciences*, *111*, 322–334.

Walter, X. A., Picazo, A., Miracle, M. R., Vicente, E., Camacho, A., Aragno, M., & Zopfi, J. (2014). Phototrophic Fe(II)-oxidation in the chemocline of a ferruginous meromictic lake. *Frontiers in Microbiology*, *5*, 1–9.

Wang, C., Konhauser, K. O., Zhang, L., Zhai, M., & Li, W. (2016). Decoupled sources of the 2.3-2.2 Ga Yuanjiacun banded iron formation: Implications for the Nd cycle in Earth's early oceans. *Precambrian Research*, *280*, 1–13.

Warchola, T., Lalonde, S. V., Pecoits, E., von Gunten, K., Robbins, L. J., Alessi, D. S., Philippot, P., & Konhauser, K. O. (2018). Petrology and geochemistry of the Boolgeeda Iron Formation, Hamersley Basin, Western Australia. *Precambrian Research*, *316*, 155–173. https://doi.org/10.1016/j.precamres.2018.07.015

Webb, G. E., & Kamber, B. S. (2000). Rare earth elements in Holocene reefal microbialites: A new shallow seawater proxy. *Geochimica et Cosmochimica Acta*, *64*, 1557–1565. https://doi.org/10.1016/S0016-7037(99)00400-7

Weyer, S., & Schwieters, J. B. (2003). High precision Fe isotope measurements with high mass resolution MC-ICPMS. *International Journal of Mass Spectrometry*, *226*, 355–368. https://doi.org/10.1016/S1387-3806(03)00078-2

Widdel, F., Schnell, S., Heising, S., Ehrenreich, A., Assmus, B., & Schink, B. (1993). Ferrous iron oxidation by anoxygenic phototrophic bacteria. *Nature*, *362*, 834–836. https://doi.org/10.1038/362834a0

Wiesli, R. A., Beard, B. L., & Johnson, C. M. (2004). Experimental determination of Fe isotope fractionation between aqueous Fe(II), siderite and "green rust" in abiotic systems. *Chemical Geology*, *211*, 343–362. https://doi.org/10.1016/j.chemgeo.2004.07.002

Wu, L., Percak-Dennett, E. M., Beard, B. L., Roden, E. E., & Johnson, C. M. (2012). Stable iron isotope fractionation between aqueous Fe(II) and model Archean ocean Fe-Si coprecipitates and implications for iron isotope variations in the ancient rock record. *Geochimica et Cosmochimica Acta*, *84*, 14–28. https://doi.org/10.1016/j.gca.2012.01.007

Wu, W., Swanner, E. D., Kleinhanns, I. C., Schoenberg, R., Pan, Y., & Kappler, A. (2017). Fe isotope fractionation during Fe(II) oxidation by the marine photoferrotroph Rhodovulum iodosum in the presence of Si – Implications for Precambrian iron formation deposition. *Geochimica et Cosmochimica Acta*, *211*, 307–321. https://doi.org/10.1016/j.gca.2017.05.033

Zhang, J., & Nozaki, Y. (1996). Rare earth elements and yttrium in seawater: ICP-MS determinations in the East Caroline, Coral Sea, and South Fiji basins of the western South Pacific Ocean. *Geochimica et Cosmochimica Acta*, *60*, 4631–4644. https://doi.org/10.1016/S0016-7037(96)00276-1

SUPPORTING INFORMATION

Additional supporting information may be found online in the Supporting Information section.

How to cite this article: Rego ES, Busigny V, Lalonde SV, et al. Anoxygenic photosynthesis linked to Neoarchean iron formations in Carajás (Brazil). *Geobiology*. 2021;19:326–341. https://doi.org/10.1111/gbi.12438